aerospace

MDPI

Article

Aerodynamic Characteristics and Static-Restoring Tendencies of a *Hopea hainanensis*-Inspired Double-Winged Samara at Different Attitudes

Xingyu Li [1] and Wei Wang [2,*]

[1] School of Aeronautic Science and Engineering, Beihang University, Beijing 100191, China; lxy24375394@buaa.edu.cn
[2] Department of Aircraft Airworthiness Certification, Civil Aviation Management Institute of China, Beijing 100102, China
* Correspondence: wangwei@camic.cn; Tel.: +86-188-2178-5826

Abstract

Low-Reynolds-number micro aerial vehicles and lightweight deployment systems require aerodynamic configurations that provide vertical support and favorable passive responses to attitude disturbances. Winged seeds delay descent through autorotation, wing curvature, and mass distribution, offering a natural model for such designs. A three-dimensional model of a *Hopea hainanensis*-inspired double-winged samara was developed, and steady multiple-reference-frame (MRF) simulations were performed at seven rotating attitudes (−45, −22.5, −10, 0, 10, 22.5, and 45 degrees) and a nonrotating 90-degree reference. Aerodynamic forces, moments, surface pressure distributions, and streamline structures were compared. Negative deflections maintained relatively high vertical support, whereas the vertical force decreased progressively with positive deflection. The −45-degree attitude combined strong vertical support, limited lateral offset, and a restoring moment increment, producing the highest equal-weight score among the rotating cases. The pitching moment response varied nonlinearly with disturbance amplitude, and the static-restoring tendency became more evident over moderate and large deflections. Surface pressure distributions, streamline structures, and the equivalent aerodynamic line of action showed that redistribution of wing loading and migration of the effective moment arm jointly governed the force and moment variations. These results characterize the quasi-steady aerodynamic response under prescribed rotation and provide guidance for the passive aerodynamic design of low-Reynolds-number aerial vehicles and lightweight deployment systems.

Keywords: *Hopea hainanensis*-inspired samara; computational fluid dynamics; multiple reference frame; quasi-steady aerodynamics; static-restoring tendency; bio-inspired aircraft

Check for updates

Academic Editor: Andrea Da-Ronch

Received: 3 August 2026
Revised: 1 September 2026
Accepted: 10 September 2026
Published: 13 September 2026

Copyright: © 2026 by the authors. Licensee MDPI, Basel, Switzerland. This article is an open access article distributed under the terms and conditions of the Creative Commons Attribution (CC BY) license.

1. Introduction

1.1. Research Background and Objectives

Low-speed, low-payload, and small-scale flight remains a central challenge in the design of micro aerial vehicles (MAVs) and bio-inspired aircraft. As the characteristic scale decreases, the flow enters the low-Reynolds-number regime, in which aerodynamic loading, flow separation, energy utilization, and disturbance response become increasingly sensitive. Under conditions with, for example, reduced air density, vertical support and propulsive efficiency may deteriorate further [1–3]. Consequently, efficient low-Reynolds-number

aerodynamic configurations and passive response designs that reduce the burden on active control have become important research directions for MAVs [4–9].

Winged seeds provide valuable natural prototypes in this context. Through autorotation, they establish stable aerodynamic structures and maintain appreciable lift at very low descent speeds [10–12]. Among such diaspores, the double-winged samara of *Hopea hainanensis* is dispersed by wind. Its gliding and autorotative characteristics demonstrate a passive low-speed flight capability produced by natural selection and may inspire the design of MAVs and lightweight bio-inspired aerial systems.

Previous studies have examined the vertical descent and autorotation of winged seeds from the perspectives of geometry, biological morphology, and aerodynamics, and have investigated how geometric parameters affect descent performance. Natural samaras, however, may assume different instantaneous orientations when exposed to atmospheric disturbances. Examining only an idealized vertical descent attitude is therefore insufficient for characterizing their stability. For an *H. hainanensis*-inspired double-winged samara, systematic comparisons of the forces, moments, and local flow fields at different prescribed attitudes remain limited.

Accordingly, this study investigates the aerodynamic characteristics of an *H. hainanensis*-inspired double-winged samara at eight prescribed attitudes. Seven rotating cases (−45, −22.5, −10, 0, 10, 22.5, and 45 degrees) resolve small, moderate, and large deflections on both sides of the 0-degree baseline, and the nonrotating 90-degree case represents broadside descent. Aerodynamic forces, moments, representative pressure distributions, and streamline structures are compared, and local regression together with multi-scale central differences is used to evaluate the quasi-steady static-restoring tendency. The results support the aerodynamic design of bio-inspired micro aerial vehicles and lightweight deployment systems.

1.2. Literature Review

Over the past decade, researchers have investigated the autorotative descent of winged seeds to address the reduced aerodynamic efficiency, increased sensitivity to turbulence, and difficulties in stability control encountered by MAVs at low Reynolds numbers. These studies have sought to explain the efficient flight mechanisms of winged seeds from aerodynamic and dynamic perspectives and to transfer the resulting principles to low-Reynolds-number aircraft.

Early investigations of aerodynamic mechanisms focused primarily on established autorotation. A broad consensus is that the leading-edge vortex formed during stable autorotation is an important contributor to the high lift produced by samaras at low descent speeds. Sunada et al. [10] reported that the descent performance of autorotating plant seeds depends not only on vertical aerodynamic force, but also strongly on lift-to-drag characteristics. Thus, delayed descent is not produced by rotation alone; instead, it results from the combined matching of geometric configuration, rotational motion, and aerodynamic loading. Subsequent sectional modeling of leading-edge vortices proposed that the additional lift generated by these structures could be incorporated into reduced-order aerodynamic models to predict the performance of autorotating samaras under different operating conditions [11]. Such work transformed a natural flight phenomenon into an engineering problem that can be quantified and parameterized.

In contrast to studies focused exclusively on stable autorotation, research on transition processes and disturbance responses has expanded in recent years. Lee and Lee [13] experimentally identified a distinct transition between release and established autorotation for maple samaras. The initial attitude affected the development of descent speed, rotational speed, and coning angle, yet stable autorotation was recovered within a relatively short

distance. Samara flight is therefore not merely a static equilibrium that exists under an ideal initial attitude; it is a dynamic process involving attitude adjustment, aerodynamic load development, and motion convergence. Ortega-Jimenez et al. [14] further showed that a large initial impulse, such as that caused by branch recoil or a gust at release, substantially changes the initial rotational frequency and deceleration process, but that the samara can nevertheless return rapidly to a near-steady autorotative descent.

Dynamic analyses have progressed from simple stability classification toward identification of the mechanisms that produce stability. Chen and Lan [15] combined morphological and kinematic parameters of maple samaras with computational fluid dynamics (CFD) estimates of stability derivatives and eigenvalue analysis. They identified several natural modes of free-falling samaras and reported that autorotation generally remained stable after a disturbance, with only limited horizontal drift. McConnell and Das [16] developed a low-order dynamic model based on blade element theory and showed that appropriate simplifications could still reproduce both steady and transient behavior. More recently, Schaeffer et al. [17] reported that maple samaras subjected to raindrop impacts may experience an instantaneous pitch deflection or local roll but generally recover autorotation rapidly, leading to a limited effect on dispersal distance.

Experimental studies have also advanced our understanding of parameter sensitivity. In vertical wind tunnel tests, Jung and Rezgui [18] systematically examined the effects of pitch and coning angles on the flight performance of natural samaras. An appropriate coning angle increased vertical thrust, whereas the maximum thrust generally occurred over a small range of pitch angles. Attitude parameters therefore govern samara aerodynamic performance. Schaeffer et al. [19] showed that maple samaras retained similar descent speeds and autorotative behavior under a range of morphological perturbations, indicating robustness to nonideal geometric variation. Hou et al. [20] subsequently demonstrated that mass distribution changes not only the center of gravity location, but also the three-dimensional descent mode, vortex structure, and aerodynamic performance.

Engineering applications have evolved from qualitative biological inspiration toward designable and optimizable configurations. Liu et al. [21] optimized a biomimetic aircraft inspired by *Pterocarya stenoptera* seeds using a neural network surrogate model and a multi-island genetic algorithm. The optimized configuration improved the aerodynamic efficiency factor by more than 50%, demonstrating that seed-inspired aircraft can be treated through parameterized optimization and data-driven design. A recent review by Arya et al. [22] further emphasized the potential of flying seed-inspired sensors and lightweight aerial nodes for environmental monitoring, precision agriculture, reforestation, and extraterrestrial exploration [22–27].

In summary, previous studies have clarified several key mechanisms associated with stable autorotation, leading-edge-vortex lift enhancement, disturbance recovery, and engineering bio-inspiration, particularly for typical single-winged maple samaras. Important gaps nevertheless remain: First, representative work has concentrated on single-winged samaras, whereas bio-inspired aerodynamic studies of Dipterocarpaceae and *H. hainanensis*-like double-winged samaras are comparatively scarce. Second, the aerodynamic responses of double-winged samaras during nonvertical descent, inclined inflow, or different spatial attitudes have not been systematically compared. Third, most studies emphasize descent speed, rotational speed, and lift-to-drag characteristics, while the aerodynamic moments and stability mechanisms of double-winged configurations at different attitudes remain insufficiently understood.

To address these gaps, the present study establishes a three-dimensional model of an *H. hainanensis*-inspired samara and performs CFD simulations at −45, −22.5, −10, 0, 10, 22.5, 45, and 90 degrees. The first seven cases share the prescribed rotational speed and represent

signed deflections of different amplitudes about the 0-degree baseline; the 90-degree case represents nonrotating broadside descent. The analysis combines aerodynamic forces and moments with representative pressure and streamline fields, local regression, multi-scale central differences, and a composite aerodynamic assessment.

2. Materials and Methods

2.1. Geometric Model and Parameter Definitions

2.1.1. Bio-Inspired Object and Modeling Strategy

A three-dimensional model was developed from an *H. hainanensis*-inspired double-winged samara and used to analyze aerodynamic performance at different prescribed attitudes. Over the past decade, studies of samaras and wind-dispersed seeds have commonly retained macroscopic aerodynamic features while simplifying fine natural surface details. This strategy preserves geometric representativeness while improving the practicality of mesh generation and numerical computation [21,28–31]. During natural descent, the two thin lateral wings primarily generate aerodynamic forces, whereas the central seed body predominantly affects mass distribution, center of gravity location, and the local flow structure. The present model therefore retains the principal aerodynamic features, including the central seed body, paired wings, bent wingtips, and wing-fold angle. Small wrinkles, irregular surface textures, and minor edge defects were simplified to improve geometric continuity and mesh quality [12]. The resulting model reproduces the overall geometry of a double-winged samara while facilitating CFD meshing, attitude transformation, and aerodynamic moment analysis.

2.1.2. Model Dimensions and Geometric Features

Figure 1 shows the three-dimensional samara model. Figure 1a–d present the isometric, top, front, and side views, respectively. The model consists of a central seed body and two thin wings that are approximately symmetric about the central plane. Preliminary measurements of the model gave an overall maximum width of 19.74 mm, a longitudinal length of 13.71 mm, and a vertical height of 14.19 mm. The projected semispan of each wing was approximately 16.2–16.9 mm, the three-dimensional root-to-tip distance was approximately 19.1–19.8 mm, and the dimensions of the central seed body were 1.58 mm × 1.28 mm × 5.51 mm.

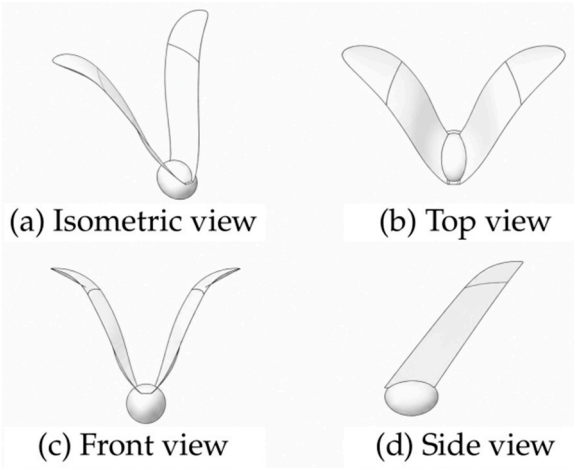

Figure 1. Three-dimensional geometric model of the *H. hainanensis*-inspired samara: (**a**) isometric view; (**b**) top view; (**c**) front view; and (**d**) side view.

The model has three primary geometric features: First, the approximately symmetric lateral wings reproduce the basic double-winged flight configuration. Second, the wingtip

regions are distinctly bent, which introduces three-dimensional camber. Third, the central seed body is ellipsoidal and affects both local flow separation and the center of gravity location. The subsequent aerodynamic analysis therefore considers not only lift and drag, but also the variation in aerodynamic moments with attitude.

2.1.3. Definition of Geometric Parameters

The principal geometric parameters used to quantify the samara shape are defined in Figure 2. The span l is the distance from the wing root to the wingtip on one side. Because the wing surface is three-dimensionally curved, the span can be represented either by its planar projection or by the three-dimensional root-to-tip distance. The projected semispan is adopted as the primary geometric parameter in Table 1, whereas the three-dimensional root-to-tip distance characterizes the actual spatial scale of the bent wing.

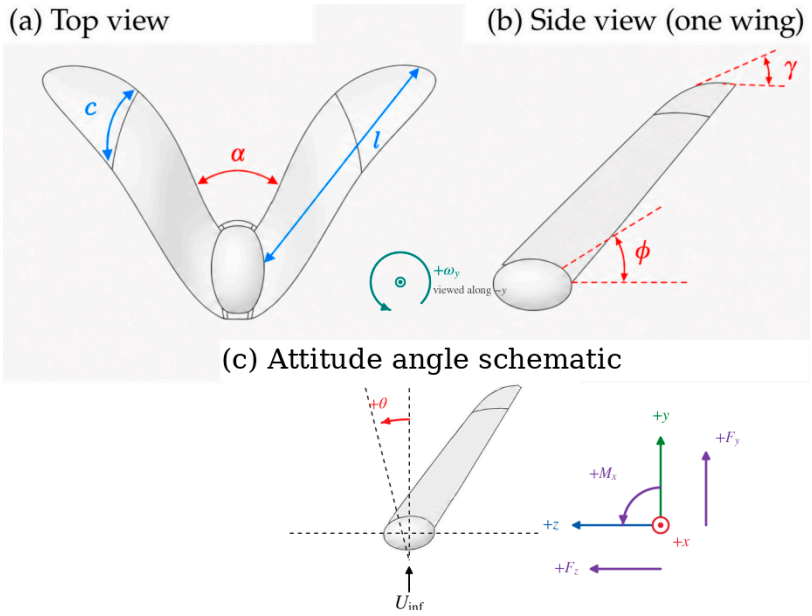

Figure 2. Definitions of the geometric parameters and attitude angle: (**a**) span l, mean chord c, and wing-fold angle α in the top view; (**b**) mounting angle ϕ and wingtip bending angle γ in the side view; and (**c**) attitude angle θ and inflow velocity U_{inf}. Dashed lines denote geometric extensions and the baseline and deflected reference directions. Straight arrows indicate positive axes and force components; curved arrows indicate positive attitude, spin, and pitching moment directions. A circled dot denotes an axis directed toward the viewer. Colors distinguish annotations only.

Table 1. Geometric and mass properties of the samara model.

Parameter	Symbol	Definition/Physical Meaning	Value	Basis/Source
Maximum lateral width	B	Maximum model envelope along the global x direction	19.74 mm	[13] (geometric context)
Envelope length in the z direction	H	Maximum model envelope along the global z direction	13.71 mm	[15] (geometric context)
Envelope height in the y direction	Z	Maximum model envelope along the global y direction	14.19 mm	[18] (geometric context)
Projected semispan	l	Planar root-to-tip distance of one wing	Approximately 16.2–16.9 mm	[28] (geometric context)

Table 1. *Cont.*

Parameter	Symbol	Definition/Physical Meaning	Value	Basis/Source
Three-dimensional root-to-tip distance	l_{3D}	Spatial root-to-tip distance of one wing	Approximately 19.1–19.8 mm	[29] (geometric context)
Mean chord	c	Average chord over several spanwise sections of one wing	3.0 mm	[21] (geometric context)
Wing-fold angle	α	Angle between the spanwise directions of the two wings	Approximately 72–75 degrees in projection; 60–62 degrees in 3D	[30] (geometric context)
Wingtip bending angle	γ	Angle between the wingtip tangent and the main wing surface extension	40–45 degrees	[31] (geometric context)
Wing area	S	Projected or actual surface area of the two wings	100 mm^2 (projected area)	[32] (geometric context)
Seed body dimensions	—	Length, width, and height of the central ellipsoidal seed body	1.58 mm × 1.28 mm × 5.51 mm	[20] (geometric context)
Uniform equivalent density	ρ_s	Uniform density calculated from the prescribed mass and model volume	4.7×10^2 kg/m^3	Calculated from m/V
Total mass	m	Representative mass based on species data and geometric scaling	0.023 g	*H. hainanensis* measurements [33]
Center of gravity location	CG	Mass centroid of the 0-degree baseline attitude	(0, 0.495, −0.322) mm	Geometric symmetry and uniform density calculation
Principal moments of inertia	(I_1, I_2, I_3)	Principal moments about the mass centroid at 0 degrees	(0.0775, 0.207, 0.226) g·mm^2	Uniform density calculation about the mass centroid
Attitude angle	θ	Counterclockwise rotation about the x axis measured from the positive y axis	−45, −22.5, −10, 0, 10, 22.5, 45, and 90 degrees	[12] (geometric context)

Note: The geometric values in Table 1 describe the present model. References in the source column provide methodological or comparative context; the values are not direct measurements reported in those studies. The representative mass is estimated from species measurements and geometric scaling as described below.

The mean chord c is the average chord measured over several spanwise sections of one wing. It is calculated from the projected area of the two wings S and the semispan l using Equation (1). The projected area is used so that the resulting mean chord is consistent with the reference scales employed for aerodynamic coefficients and wing loading.

$$c = \frac{S}{2l} \tag{1}$$

The wing-fold angle α is the angle between the spanwise directions of the two wings. Because the model is a three-dimensional curved surface, this angle may be defined either from the top view projection or from the three-dimensional span vectors. The present study primarily uses the angle between the projected spans in the top view. Previous studies of double-winged autorotating seeds have shown that the wing-fold angle and wing curvature significantly affect terminal descent speed, autorotative behavior, and aerodynamic efficiency [30,31]. Preliminary measurements gave a projected wing-fold angle of approximately 72–75 degrees and a three-dimensional angle of approximately 60–62 degrees. A consistent definition is used in all subsequent calculations to ensure comparability among attitudes.

The wingtip bending angle γ describes the deflection of the terminal wing segment relative to the approximately straight region near the root. Specifically, γ is defined as the angle between the tangent to the bent wingtip segment and the primary extension direction of the wing surface. The current model has a distinct downward bend with an equivalent angle of approximately 40–45 degrees. Wing surface curvature and wingtip bending modify the local angle of attack, vortex structures, and surface pressure distribution and are important determinants of the lift and descent performance of autorotating samaras [30–32].

The mounting angle ϕ is the angle between the root chord and the model reference axis. Because the mounting angle, inflow direction, rotation axis, and attitude angle all depend on the coordinate system, the global axes shown in Figure 3 are used throughout this study. The positive y direction is vertically upward and aligned with the inlet flow, the positive z direction points horizontally to the left in the illustrated view, and the positive x direction is normal to the illustrated $y - z$ plane. The positive axes follow the Fluent coordinate markers in Figure 3. The prescribed rotation cases rotate about the y axis, whereas attitude deflection is defined about the x axis.

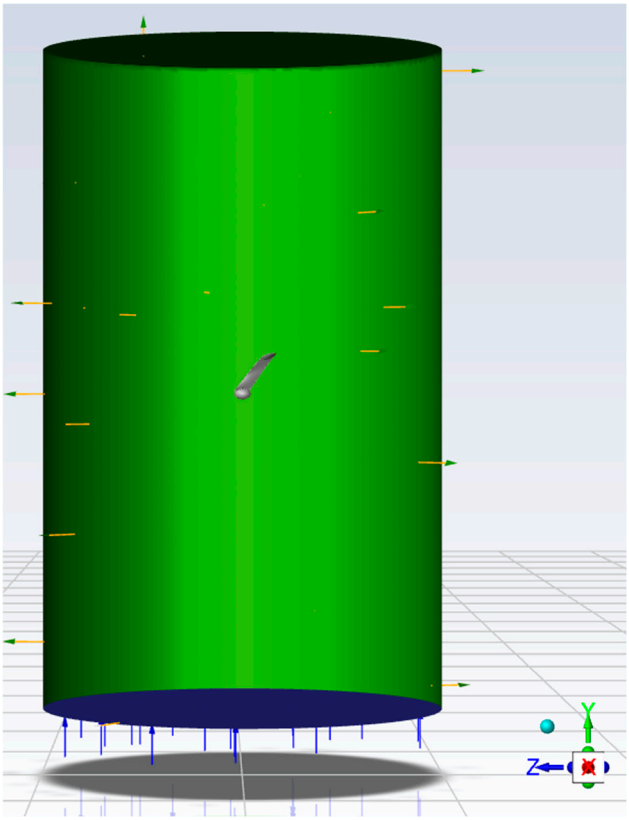

Figure 3. Fluent computational domain, local rotating domain, and boundary directions. The green cylinder is the outer computational domain. The coordinate markers indicate the positive global axes: $+y$ is upward, $+z$ points leftward in the illustrated view, and $+x$ is normal to the $y - z$ plane. The prescribed rotation cases rotate about the y axis, and the attitude angle is defined as a counterclockwise rotation about the x axis. The small colored spheres and arrows are software orientation markers, not additional physical bodies or flow features.

2.1.4. Definition of Attitude Angle

The attitude angle θ describes the orientation of the double-winged samara. A positive angle is defined as a counterclockwise rotation of the model reference direction about the x axis, measured from the positive y axis, and the baseline is θ = 0 degrees. Eight prescribed attitudes were analyzed in the following order: -45, -22.5, -10, 0, 10, 22.5, 45, and 90 degrees. The first seven cases used the common prescribed rotation, whereas

the 90-degree case was nonrotating. The angle definition and positive direction follow Figures 2 and 3.

The eight attitudes span different disturbance directions and amplitudes about the 0-degree baseline. At $|\theta| = 45$ degrees, the model reference direction has equal-magnitude projections along the y and z axes. Further deflection makes the z-direction projection larger than the vertical projection and moves the configuration toward the 90-degree broadside condition. The −45- and 45-degree cases therefore form the negative and positive limits of the rotating attitude series. The −22.5- and 22.5-degree cases represent moderate disturbances, and the −10- and 10-degree cases represent small symmetric disturbances. This sequence supports a five-point local regression from −22.5 to 22.5 degrees and central difference comparisons at ±10, ±22.5, and ±45 degrees. The nonrotating 90-degree case represents broadside descent with the model reference direction normal to +y.

The 0-degree attitude is defined as the kinematic baseline because the model reference direction, inlet flow, and prescribed spin axis all coincide with the positive y axis, and the paired wings assume their fully deployed rotating descent configuration. The remaining rotating attitudes are expressed as signed deflections from this common geometric and kinematic state. Experiments have shown that release attitude affects the development of rotational speed, descent velocity, and coning angle, that strong initial disturbances alter transient deceleration, and that pitch and coning angles influence vertical aerodynamic loading [13,14,18]. The ±10-, ±22.5-, and ±45-degree pairs represent small, moderate, and large deflections, respectively. The finite baseline moment, $M_x(0) = 1.5341 \times 10^{-6}$ N m, is retained at the 0-degree kinematic reference, and the quasi-steady static-restoring tendency is evaluated from moment increments and multi-scale central differences relative to this state.

The disturbance response analysis uses the signed equivalent angles $\theta_e = -45$, −22.5, −10, 0, 10, 22.5, and 45 degrees about the 0-degree baseline. Local regressions and aerodynamic derivatives are calculated from these seven prescribed rotation cases. The 90-degree case is treated separately as the nonrotating broadside reference.

Table 1 summarizes the principal geometric parameters and the mass properties of the 0-degree baseline model. The geometric quantities were obtained from the three-dimensional model. Published measurements of *H. hainanensis* samaras give a mean intact fruit mass of 0.87 g, a mean wing area of 12.83 cm^2, and a fruit mass coefficient of variation of 24.1% [33]. Geometric scaling to the present 1.00 cm^2 reference area gives a mass estimate of approximately 0.019 g. The representative model mass was set to m = 0.023 g, consistent with the reported intraspecific variation. The model volume is 49.2 mm^3, corresponding to a uniform equivalent density of $\rho_s = 4.7 \times 10^2$ kg/m^3. Under the uniform density assumption, symmetry about the y–z plane gives a zero x-coordinate for the mass centroid; the remaining centroid coordinates and principal moments of inertia were evaluated from the model geometry. The values used in subsequent calculations are listed in Table 1.

2.2. Numerical Simulation Method

Recent studies of winged seeds have generally followed a common numerical workflow: A real or simplified three-dimensional model is first constructed from the natural geometry, and key quantities such as the span, chord, fold angle, bending angle, mass distribution, and center of gravity location are extracted. A locally refined computational domain is then established around the rotating samara, and the aerodynamic loads and flow field are obtained using the Navier–Stokes or Reynolds-averaged Navier–Stokes equations together with a moving reference frame, prescribed rotation, or a transient rotating mesh. Finally, local refinement, near-wall prism layers, and grid independence tests are used to establish numerical reliability [21,28–32,34].

2.2.1. Computational Domain and Boundary Conditions

An external flow domain and an internal rotating subdomain were constructed to investigate the prescribed attitudes, and the geometric model was imported into Ansys Fluent. Recent numerical studies of samaras commonly combine an external domain with a high-resolution region near the seed to limit far-field boundary effects while resolving flow details adjacent to the wings [21,28,29,32,34]. The computational domain consists of a stationary outer region and an inner rotating region that encloses the samara, with data transferred across their interface. The stationary outer domain is cylindrical, with a radius of 67.5 mm and an axial length of 222.29 mm. The inner rotating domain is also cylindrical, with a radius of 17.5 mm and an axial length of 22.29 mm. The seed model is located within the rotating domain to provide higher spatial resolution in its immediate vicinity.

The inlet was specified as a velocity inlet with a magnitude of 1.8 m/s directed along the positive global y axis. The outlet was specified as a pressure outlet with a gauge pressure of 0 Pa. A no-slip wall condition was imposed on the seed surface to calculate the aerodynamic forces. At both the inlet and outlet, the turbulence conditions were defined by a turbulence intensity of 5% and a turbulent viscosity ratio of 10. Air was treated as an incompressible Newtonian fluid with a density of 1.225 kg/m^3 and a dynamic viscosity of 1.7894×10^{-5} kg/(m s). Figure 3 shows the computational domain and boundary directions in Fluent. The principal numerical simulation settings are summarized in Table 2. Gravity was disabled in Fluent; the body weight W = mg was introduced in postprocessing along −y for comparison with the vertical aerodynamic force Fy.

Table 2. Principal numerical simulation settings.

Item	Setting
Solver	Pressure-based, steady, absolute velocity formulation
Fluid	Air, $\rho = 1.225$ kg/m^3, $\mu = 1.7894 \times 10^{-5}$ kg/(m s)
Outer domain	Stationary cylinder, radius 67.5 mm, axial length 222.29 mm
Inner domain	Rotating cylinder, radius 17.5 mm, axial length 22.29 mm
Inlet	Velocity inlet, $U = 1.8$ m/s, direction $+y$
Outlet	Pressure outlet, gauge pressure 0 Pa
Wall	Seed surface, seed_wall
Turbulence model	k–ω SST
Inlet turbulence	Turbulence intensity 5%, turbulent viscosity ratio 10

2.2.2. MRF Rotating Domain Setting

The multiple-reference-frame (MRF) method was used to represent the mean rotational effect at a prescribed angular velocity. Previous numerical studies of autorotating samaras have used moving reference frames, prescribed rotation, or steady rotating approximations to obtain mean aerodynamic forces and flow structures [28,29,32,34]. Comparisons of rotating machinery methods also indicate that the MRF method can provide time-averaged loads at relatively low computational cost, whereas sliding meshes are more suitable for resolving blade-passing events, periodic interactions, and transient fluctuations [35,36]. The MRF axis of the inner domain passes through the global origin (0, 0, 0) and is directed along +y.

The immediate objective of this study was to screen several discrete attitudes under identical inflow, rotational speed, and geometric conditions and to compare the corresponding mean forces, mean moments, and flow organization. A transient sliding mesh resolves physical mesh rotation and requires small-time-step advancement, whereas the MRF method represents the mean rotational effect on a stationary mesh and substantially reduces computational cost. A six-degrees-of-freedom (6DOF) analysis additionally requires reliable mass properties, moments of inertia, free-motion constraints, and dynamic

mesh settings and resolves the time evolution of free-flight attitude. The MRF method is appropriate for the first-stage parametric screening performed in this study.

At each attitude, the MRF method keeps the model fixed relative to the rotating domain and represents the mean effect of the prescribed rotational speed in a steady rotating frame. This formulation is suited to comparisons of mean loads and principal flow structures under common inflow, rotational speed, and geometric conditions. The resulting forces and moments are quasi-steady responses at the prescribed attitudes and angular velocity. Rotational speed development, unsteady wake evolution, attitude–speed coupling, and recovery trajectories in free descent require transient sliding-mesh or 6DOF calculations and free-descent experiments. The moment increments and aerodynamic stiffness reported here therefore characterize a quasi-steady static-restoring tendency.

An angular velocity of ω = 4 rad/s was applied consistently to the seven prescribed rotation cases at −45, −22.5, −10, 0, 10, 22.5, and 45 degrees. To quantify the relative time scales of rotation and translational inflow, the rotational frequency, convective time for the flow to traverse one characteristic length, complete rotational period, and Strouhal number are defined by Equations (2)–(5). Here, l is the characteristic length and U is the inflow velocity. The Strouhal number couples prescribed angular velocity, model scale, and inflow velocity in a single dimensionless parameter and compares the time required for convection over one characteristic length with that required for one complete rotation.

$$f = \frac{\omega}{2\pi} \tag{2}$$

$$t_c = \frac{l}{U} \tag{3}$$

$$T_r = \frac{1}{f} = \frac{2\pi}{\omega} \tag{4}$$

$$St = \frac{fl}{U} = \frac{\omega l}{2\pi U} = \frac{t_c}{T_r} \tag{5}$$

Rotation–translation coupling can also be interpreted through the angle accumulated by the model during one convective time, as defined by Equation (6). With l = 16.55 mm, U = 1.8 m/s, and ω = 4 rad/s, the present values are f = 0.637 Hz, tc = 0.00919 s, Tr = 1.571 s, and St = 0.00585. The corresponding accumulated angle is 0.0368 rad, or approximately 2.11 degrees. Using the reference rotational radius R = 19.45 mm, the wingtip tangential speed is 0.0778 m/s and the tip–speed ratio is 0.0432. These measures place all seven prescribed rotation cases in a low-rotation-coupling regime dominated by translational inflow. Applying the same rotational input across the seven attitudes therefore isolates attitude effects while holding the rotation–translation coupling level constant. The 90-degree case has zero angular velocity and serves only as a nonrotating reference.

An angular velocity of ω = 4 rad/s was adopted as the common prescribed speed for the seven rotating attitudes, providing a consistent rotation–translation coupling level for isolating the effect of attitude. The resulting Strouhal number S_t = 0.00585, angular displacement over one convective time of 0.0368 rad (2.11 degrees), and tip–speed ratio of 0.0432 characterize a weak rotational coupling. To assess this choice, the 0-degree baseline was evaluated at ω = 2, 4, 6, and 15 rad/s with the same mesh, boundary conditions, and SST settings; these cases span S_t = 0.00293–0.02195 and tip–speed ratios of 0.0216–0.162.

$$\Delta\psi_c = \omega t_c = 2\pi St \tag{6}$$

$$\lambda = \frac{\omega R}{U} \tag{7}$$

2.2.3. Nondimensionalization and Reference Scales

The projected area of both wings $S = 100$ mm^2, mean chord $c = 3.0$ mm, mean projected semispan $l = 16.55$ mm, and mean three-dimensional root-to-tip distance $R = 19.45$ mm were adopted as reference scales. The dynamic pressure, chord-based Reynolds number, span-based Reynolds number, reduced rotational speed, and geometric aspect ratio were calculated from Equations (8)–(12). The Strouhal number and tip–speed ratio were calculated from Equations (5) and (7), respectively. Aerodynamic force and moment coefficients are defined in Section 3.3. Table 3 summarizes the reference quantities and dimensionless parameters.

$$q = \frac{\rho U^2}{2} \tag{8}$$

$$Re_c = \frac{\rho U c}{\mu} \tag{9}$$

$$Re_l = \frac{\rho U l}{\mu} \tag{10}$$

$$k = \frac{\omega c}{2U} \tag{11}$$

$$AR = \frac{B^2}{S} \tag{12}$$

Table 3. Reference quantities and dimensionless parameters.

Parameter	Symbol/Formula	Value
Inlet velocity	U	1.8 m/s
Reference area	S	1.00×10^{-4} m^2
Reference chord	c	3.00×10^{-3} m
Mean projected semispan	l	1.655×10^{-2} m
Mean rotational radius	R	1.945×10^{-2} m
Dynamic pressure	$q = \rho U^2/2$	1.9845 Pa
Chord Reynolds number	$Re_c = \rho U c/\mu$	370
Span Reynolds number	$Re_l = \rho U l/\mu$	2039
Strouhal number	$St = fl/U$	0.0059
Tip–speed ratio	$\lambda = \omega R/U$	0.0432
Reduced rotational speed	$k = \omega c/(2U)$	0.0033
Geometric aspect ratio	$AR = B^2/S$	3.90

The chord-based Reynolds number is $Re_c \approx 370$, placing the model in a characteristic low-Reynolds-number regime. The span-based value is $Re_l \approx 2.04 \times 10^3$, indicating that appreciable inertia-dominated separation and rotation-induced flow structures may nevertheless form at the wing scale.

2.2.4. Mesh Generation

Because the samara wings exhibit substantial curvature variation and pronounced separation may occur near the roots and tips, the region adjacent to the model and the internal rotating domain were locally refined. Numerical studies of autorotating samaras commonly refine the wing surface, root, and tip regions to resolve leading-edge, wingtip, and separated vortices [21,28,32,34]. The overall mesh combines tetrahedral elements in the main flow region with near-wall prism layers that resolve the velocity gradients and boundary-layer structure adjacent to the seed surface.

Following the grid independence assessment in Section 2.2.6, mesh G2 with 7,654,300 volume cells was adopted for the multi-attitude simulations. The mesh combines

tetrahedral cells in the main flow region with local refinement in the internal rotating domain and around the wing roots and tips. Ten prism layers were generated on seed_wall with a growth rate of 1.2 and a total thickness of 9.3×10^{-2} mm. Figures 3–5 show the computational domain, global mesh, and local refinement, and Table 4 summarizes the principal mesh characteristics.

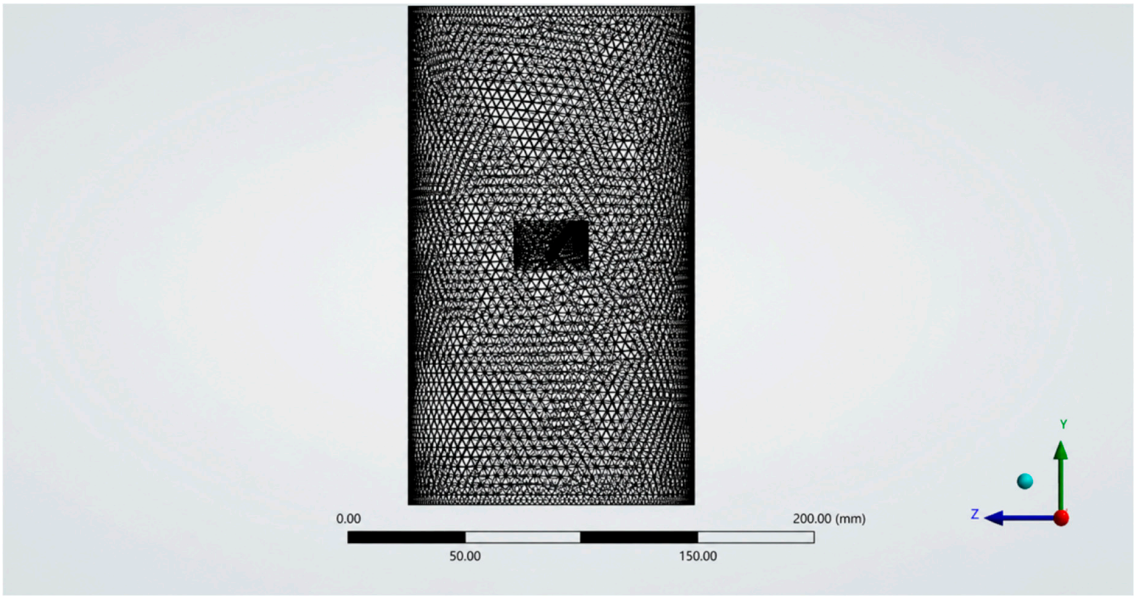

Figure 4. Global computational mesh showing the outer flow domain, the locally refined inner region, and the position of the samara model. The colored spheres and arrows at the lower right are orientation markers; gray shading provides the mesh-view background.

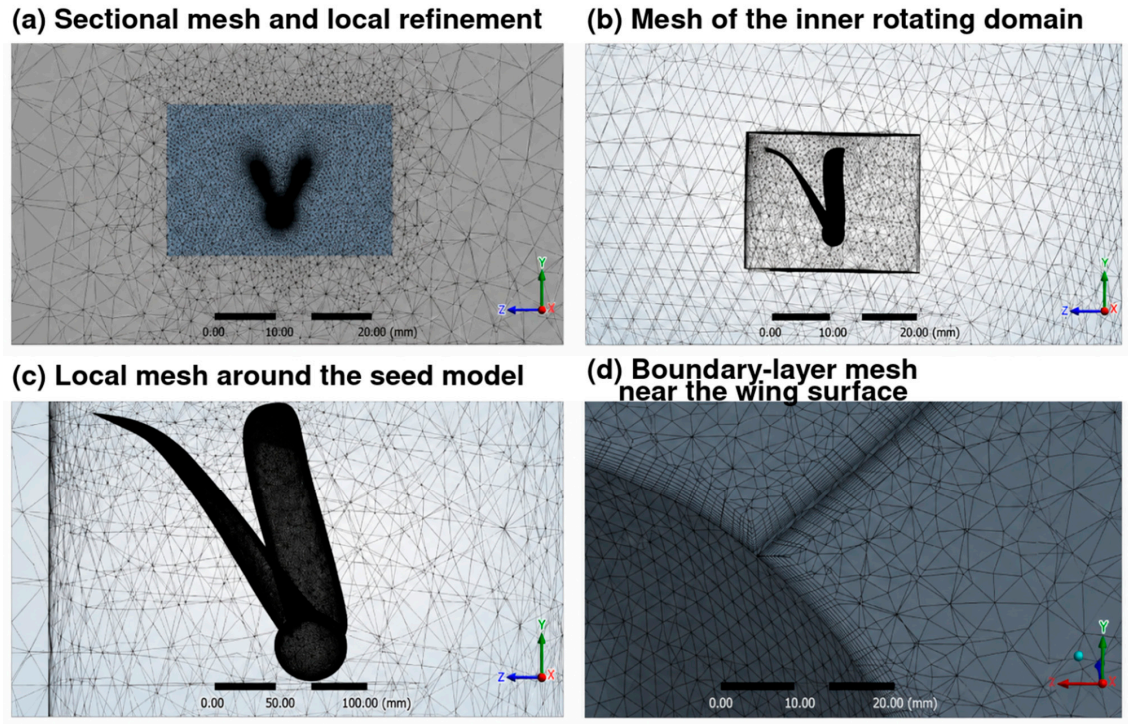

Figure 5. Mesh details: (**a**) sectional mesh and local refinement; (**b**) mesh of the inner rotating domain; (**c**) local mesh around the samara model; and (**d**) boundary-layer mesh adjacent to the wing surface. Small colored spheres and arrows denote the viewing coordinate system. Shaded surfaces distinguish the samara and the displayed mesh regions, rather than physical flow quantities.

Table 4. Mesh characteristics used for the multi-attitude simulations.

Item	Value/Setting
Total number of volume cells	7,654,300
Element types	Tetrahedral cells with near-wall prism layers
Locally refined regions	Inner rotating domain, wing roots, and wingtips
Boundary-layer surface	seed_wall
Number of prism layers	10
Prism-layer growth rate	1.2
Total prism-layer thickness	9.3×10^{-2} mm

2.2.5. Discretization Schemes and Aerodynamic Load Output

The governing equations were the steady Reynolds-averaged Navier–Stokes (RANS) equations, closed with the k–ω SST model. Its near-wall k–ω formulation and shear stress transport limiter provide sensitivity to wall shear, adverse pressure gradients, and separated flow [37]. The same closure has been used in numerical studies on autorotating maple and *Tristellateia* seeds and on a maple samara-inspired wing [32,34,38]. All attitude cases were solved within a common MRF–RANS framework, and the resulting loads and flow structures characterize quasi-steady responses under the prescribed conditions.

Pressure–velocity coupling was performed with the Coupled algorithm. Gradients were evaluated using the Least-Squares Cell-Based method, pressure was discretized with a Second-Order scheme, and the momentum, turbulent kinetic energy, and specific dissipation rate equations were discretized using Second-Order Upwind schemes.

The resultant pressure and viscous forces on seed_wall were monitored during the calculations. The positive directions of the global aerodynamic force components follow Figure 3. The component F_y acts along +y and represents lift or vertical support in all eight cases; F_z acts along +z and represents the lateral aerodynamic force associated with transverse drift. The moments M_x, M_y, and M_z are evaluated about the mass centroid of the corresponding attitude and follow the right-hand rule. The centroid listed in Table 1 applies to the 0-degree model. Because geometry and material distribution remain unchanged, the centroid is transformed with the model before moment integration at each attitude, giving all cases a consistent centroid-based moment definition.

2.2.6. Grid Independence Assessment

Six meshes with different cell counts were tested to evaluate the sensitivity of the integrated aerodynamic force and pitching moment to grid resolution. Geometry, computational domain, boundary conditions, angular velocity, and solver settings were held constant. The monitored quantities were the vertical force F_y and pitching moment coefficient $Cmx = M_x/(qSc)$, where M_x is evaluated about the mass centroid and q = 1.9845 Pa, $S = 1.00 \times 10^{-4}$ m^2, and $c = 3.00 \times 10^{-3}$ m. Table 5 lists F_y, M_x, Cmx, and the Cmx deviation from the finest mesh G5. Figure 6 compares the two grid-dependence trends.

There are appreciable F_y fluctuations when the mesh count is below or near 6.0×10^6. Above approximately 6.0×10^6 cells, F_y remains primarily within 2.13×10^{-4}–2.25×10^{-4} N, indicating a diminishing influence of further refinement on the principal aerodynamic force. The pitching moment coefficient follows the same convergence pattern: G6, G3, and G1 give Cmx = 2.5581–2.5768, while G2–G5 give 2.6652–2.6873. Relative to G4 and G5, the G2 values differ by 0.82% and 0.63% for Cmx and by 0.26% and 0.60% for F_y, respectively. Both integrated-load metrics therefore change by less than 1% between G2 and the finer meshes. Considering numerical accuracy and computational cost, G2 with 7.6543×10^6 cells was selected for the subsequent multi-attitude simulations.

Table 5. Grid independence results based on vertical force and the pitching moment coefficient.

Mesh	Cells ($\times 10^6$)	F_y ($\times 10^{-4}$ N)	M_x ($\times 10^{-6}$ N·m)	*Cmx*	*Cmx* Deviation from G5 (%)
G6	5.9892	2.1308	1.5303	2.5704	4.17
G3	6.2520	2.1274	1.5229	2.5581	4.63
G1	6.6849	2.1792	1.5341	2.5768	3.93
G2 (selected)	7.6543	2.2363	1.5867	2.6652	0.63
G4	9.3035	2.2422	1.5999	2.6873	0.19
G5	11.9493	2.2498	1.5968	2.6821	—

Note: The meshes are ordered by increasing cell count. $Cmx = M_x/(qSc)$. The last column gives the absolute *Cmx* deviation relative to the finest mesh G5. G2 was selected for the subsequent simulations. The em dash denotes the reference mesh itself, for which a relative deviation is not applicable.

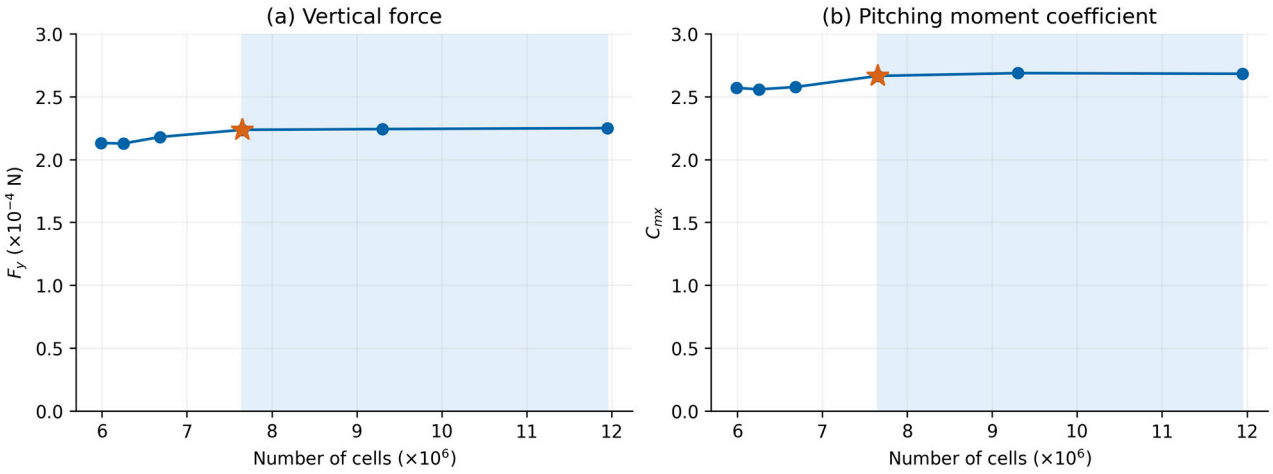

Figure 6. Grid independence assessment based on (**a**) vertical force F_y and (**b**) pitching moment coefficient *Cmx*. The star denotes the selected G2 mesh, and the shaded region covers G2 and the finer meshes.

2.2.7. Iterative Convergence Assessment

Iterative convergence was evaluated jointly from the equation residuals and the integrated force history. Figure 7 presents scaled residuals for the representative $-45°$, $0°$, $45°$, and $90°$ cases together with the vertical aerodynamic force F_y monitored at $0°$. After the initial adjustment, the momentum equation residuals remained on the order of 10^{-4} and the specific dissipation rate residual on the order of 10^{-5}; the continuity and turbulent kinetic energy k residuals reached stationary plateaus on the order of 10^{-1} and 10^{-2}, respectively. At $0°$, F_y approached a stable value of approximately 2.2×10^{-4} N after about 100 iterations and showed no systematic drift thereafter. The residual histories of these representative cases reached stationary plateaus before load extraction, and the $0°$ F_y history remained stable over the corresponding final interval.

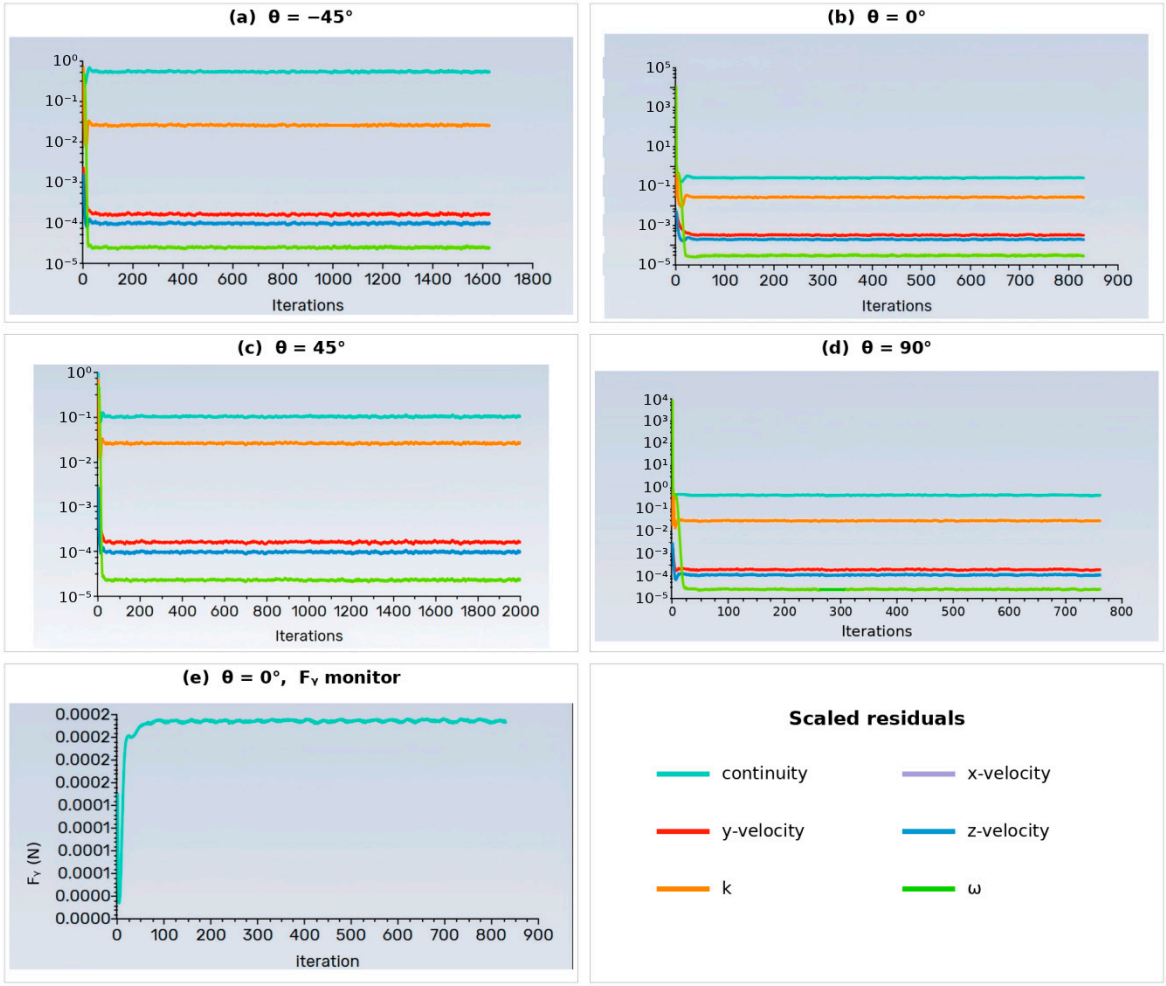

Figure 7. Iteration histories for representative attitudes: scaled residuals at (**a**) −45°, (**b**) 0°, (**c**) 45°, and (**d**) 90°; and (**e**) vertical aerodynamic force F_y at 0°.

3. Results and Discussion

3.1. Aerodynamic Forces at Different Attitudes

Table 6 lists the aerodynamic force components in ascending attitude order. Across the seven rotating cases, F_y remains on a high plateau from −45 to −10 degrees (2.3308–2.3617 × 10^{-4} N) and then decreases progressively through 0, 10, 22.5, and 45 degrees. Relative to 0 degrees, F_y changes by +5.46%, +5.61%, +4.23%, −7.40%, −25.57%, and −76.20% at −45, −22.5, −10, 10, 22.5, and 45 degrees, respectively. This ordered trend shows that positive attitude deflection progressively reduces the effective windward projection and cooperative loading of the paired wings, whereas moderate negative deflection preserves vertical support. The lateral component F_z evolves differently: it is nearly zero at −45 degrees, increases through −22.5, −10, 0, and 10 degrees, reaches 1.1129 × 10^{-4} N at 22.5 degrees, and then decreases at 45 degrees as the total aerodynamic loading collapses. The nonrotating 90-degree reference has F_y = 8.0640 × 10^{-5} N and F_z = −1.1141 × 10^{-4} N, indicating a distinct broadside loading mode dominated by transverse drift.

Table 6. Aerodynamic force components at the eight prescribed attitudes.

Case	Attitude θ	Condition	F_y (N)	F_z (N)	Principal Observation
Case 1	−45 degrees	Rotating	2.3583×10^{-4}	-2.3398×10^{-6}	High support; minimum lateral offset
Case 2	−22.5 degrees	Rotating	2.3617×10^{-4}	2.0928×10^{-5}	Maximum F_y among rotating cases
Case 3	−10 degrees	Rotating	2.3308×10^{-4}	5.6883×10^{-5}	High support near baseline
Case 4	0 degrees	Rotating baseline	2.2363×10^{-4}	7.9489×10^{-5}	Kinematic reference
Case 5	10 degrees	Rotating	2.0707×10^{-4}	1.0327×10^{-4}	Support decreases; lateral load rises
Case 6	22.5 degrees	Rotating	1.6645×10^{-4}	1.1129×10^{-4}	Largest positive F_z
Case 7	45 degrees	Rotating	5.3213×10^{-5}	2.9011×10^{-5}	Marked support loss
Case 8	90 degrees	Nonrotating reference	8.0640×10^{-5}	-1.1141×10^{-4}	Broadside transverse loading

Using the representative mass m = 0.023 g in Table 1 and g = 9.81 m/s^2 gives a model weight W = 2.26×10^{-4} N. At 0 degrees, Fy = 2.24×10^{-4} N and Fy/(mg) = 0.991, corresponding to a 0.89% difference between the vertical aerodynamic force and weight. This condition therefore approaches vertical force balance at the prescribed inflow speed and rotation rate. The corresponding pitching moment is Mx = 1.53×10^{-6} N·m, and the 0-degree condition serves as the kinematic baseline for the prescribed attitude comparison. A free equilibrium attitude is determined by simultaneous force and moment balance.

The eight cases exhibit a continuous and asymmetric attitude response. From −45 to −10 degrees, F_y remains high, and negative deflection substantially reduces the lateral offset relative to the 0-degree baseline. Positive deflection increases the lateral share of the resultant load and culminates in a marked loss of total loading at 45 degrees. The −45-degree attitude combines $F_y = 2.3583 \times 10^{-4}$ N with a near-zero F_z, while the −22.5-degree case gives the maximum rotating case $F_y = 2.3617 \times 10^{-4}$ N. Figure 8 compares the force components for all eight attitudes.

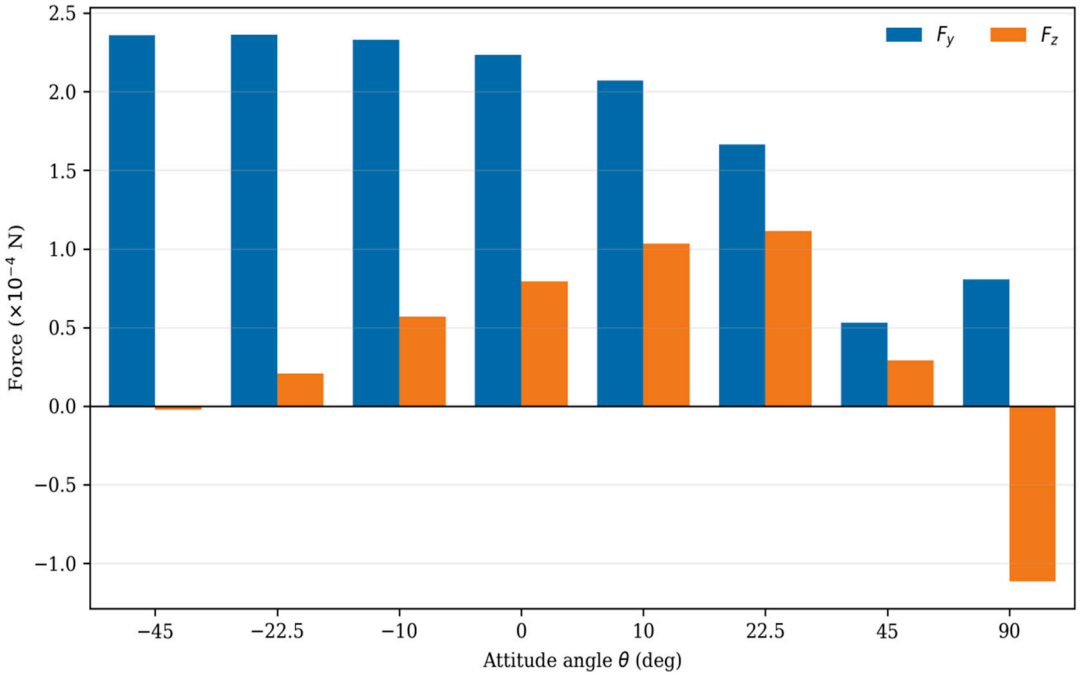

Figure 8. Aerodynamic force components at the eight prescribed attitudes, ordered from −45 to 90 degrees.

The rotational speed sensitivity at the 0-degree baseline was evaluated at 2, 4, 6, and 15 rad/s. Across this range, $F_y = 2.1922 \times 10^{-4}$–$2.2363 \times 10^{-4}$ N, $F_z = 7.9489 \times 10^{-5}$–$8.2535 \times 10^{-5}$ N, and $M_x = 1.5341 \times 10^{-6}$–$1.5935 \times 10^{-6}$ N m. Relative to the 4 rad/s

case, the maximum deviations were 1.97%, 3.83%, and 3.87%, respectively. The vertical force decreased only slightly at 15 rad/s, whereas F_z and M_x varied nonmonotonically. The limited variation of the mean loads over the tested range supports the common use of 4 rad/s as a prescribed speed for comparing attitude effects.

3.2. Aerodynamic Moments and Static Pitch-Restoring Tendency

Table 7 and Figure 9 present the aerodynamic moments about the mass centroid. M_x is predominantly on the order of 10^{-6} N m, whereas M_y and M_z are mainly on the order of 10^{-8} N m; the pitching moment about the x axis therefore governs the attitude response. The seven rotating values of M_x are positive and nonmonotonic. M_x decreases from 1.7122×10^{-6} N m at −45 degrees to 1.5341×10^{-6} N m at 0 degrees, increases to 1.5836×10^{-6} N m at 10 degrees, and then decreases to 1.3948×10^{-6} and 8.9814×10^{-7} N m at 22.5 and 45 degrees. The shallow local reversal near 0 degrees demonstrates a nonlinear, disturbance amplitude-dependent pitching moment response.

Table 7. Aerodynamic moments about the mass centroid at the eight prescribed attitudes.

Case	Attitude θ	M_x (N m)	M_y (N m)	M_z (N m)	Moment Increment Interpretation
Case 1	−45 degrees	1.7122×10^{-6}	-7.6786×10^{-9}	-5.2369×10^{-9}	Restoring increment
Case 2	−22.5 degrees	1.6145×10^{-6}	-4.3590×10^{-9}	1.0226×10^{-8}	Restoring increment
Case 3	−10 degrees	1.5686×10^{-6}	-2.4808×10^{-9}	-9.8160×10^{-9}	Restoring increment
Case 4	0 degrees	1.5341×10^{-6}	1.2047×10^{-8}	3.5485×10^{-8}	Baseline moment
Case 5	10 degrees	1.5836×10^{-6}	-9.4370×10^{-9}	-1.1799×10^{-8}	Non-restoring increment
Case 6	22.5 degrees	1.3948×10^{-6}	8.7049×10^{-10}	3.8601×10^{-9}	Restoring increment
Case 7	45 degrees	8.9814×10^{-7}	-1.6425×10^{-8}	1.1793×10^{-8}	Restoring increment
Case 8	90 degrees	-9.5631×10^{-7}	-6.0091×10^{-9}	1.1862×10^{-10}	Nonrotating reference

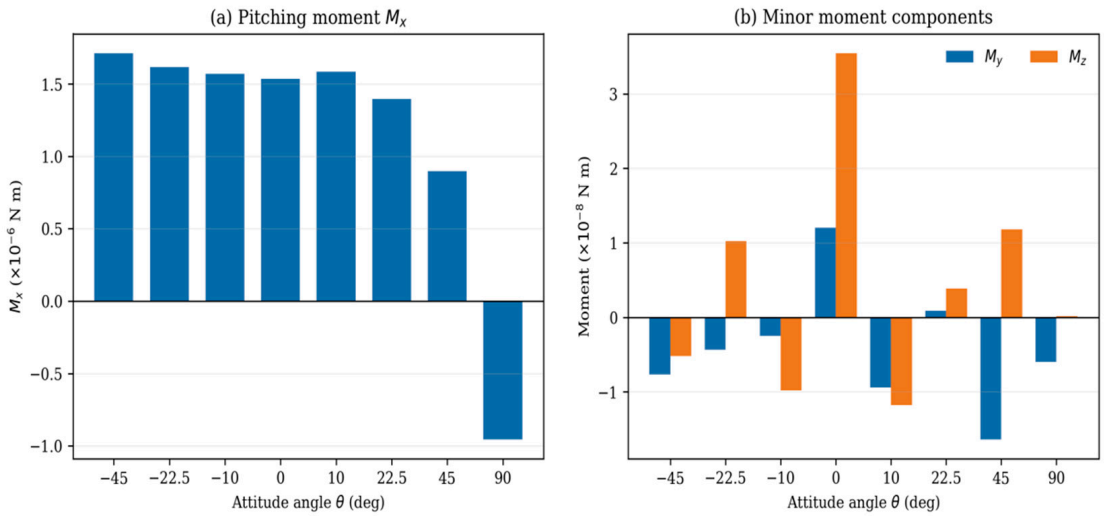

Figure 9. Aerodynamic moments about the mass centroid at the eight prescribed attitudes: (**a**) pitching moment M_x; and (**b**) minor components M_y and M_z.

At the integrated-load level, M_x is governed by the effective moment arm of the y–z resultant force about the mass centroid. The reported F_y, F_z, and M_x values define the minimum-distance point on an equivalent line of action in the y–z plane; Section 3.3 gives its formulation and numerical values. The decrease in M_x from −45 to 0 degrees and its local rise at 10 degrees show that the resultant force direction and effective moment arm vary jointly with attitude. Relative to the 0-degree baseline, moment increments oppose the disturbance at −45, −22.5, −10, 22.5, and 45 degrees, while the 10-degree increment acts in

the disturbance direction. The quasi-steady static-restoring tendency therefore varies with disturbance amplitude.

The nonrotating 90-degree case has a negative M_x, reflecting the change in windward exposure and resultant force position during broadside descent. This case is treated separately as the nonrotating reference. The much smaller M_y and M_z components change sign among attitudes, while M_x remains the governing moment. Section 3.3 quantifies the pitching response of the seven rotating cases through multi-scale central differences.

3.3. Dimensionless Attitude Response and Local Aerodynamic Derivatives

The equivalent disturbance angle θ_e is used to order the seven prescribed rotation cases directly as −45, −22.5, −10, 0, 10, 22.5, and 45 degrees. The 90-degree case remains a nonrotating broadside reference and is excluded from regression and derivative calculations because its rotation–translation coupling differs from that of the rotating series. This distinction limits the following analysis to quasi-steady prescribed attitude responses about the 0-degree kinematic baseline.

To remove the direct influence of air density, inflow speed, reference area, and model scale, the dynamic pressure from Equation (8), reference area S, and reference chord c are used to nondimensionalize the forces and pitching moment. The vertical force coefficient, lateral force coefficient, resultant force coefficient in the y–z plane, and pitching moment coefficient about the x axis are defined by Equations (13)–(16):

$$C_Y = \frac{F_y}{qS} \tag{13}$$

$$C_Z = \frac{F_z}{qS} \tag{14}$$

$$C_R = \sqrt{C_Y^2 + C_Z^2} \tag{15}$$

$$C_{mx} = \frac{M_x}{qSc} \tag{16}$$

Here, C_R represents the magnitude of the resultant of F_y and F_z in the y–z plane and contains no directional information. With ρ = 1.225 kg/m^3, U = 1.8 m/s, S = 1.00 × 10^{-4} m^2, and c = 3.00 × 10^{-3} m, q = 1.9845 Pa, qS = 1.9845 × 10^{-4} N, and qSc = 5.9535 × 10^{-7} N m. At 0 degrees, for example, C_Y = 1.1269, C_Z = 0.4005, C_R = 1.1960, and C_{mx} = 2.5768. Table 8 reports the coefficients for all seven prescribed rotation attitudes.

Table 8. Dimensionless aerodynamic force and pitching moment coefficients for the seven prescribed rotation attitudes.

Case	θ_e	C_Y	C_Z	C_R	C_{mx}
Case 1	−45 degrees	1.1884	−0.0118	1.1884	2.8760
Case 2	−22.5 degrees	1.1901	0.1055	1.1947	2.7119
Case 3	−10 degrees	1.1745	0.2866	1.2090	2.6348
Case 4	0 degrees	1.1269	0.4005	1.1960	2.5768
Case 5	10 degrees	1.0434	0.5204	1.1660	2.6599
Case 6	22.5 degrees	0.8388	0.5608	1.0090	2.3428
Case 7	45 degrees	0.2681	0.1462	0.3054	1.5086

The five cases at −22.5, −10, 0, 10, and 22.5 degrees form the local sample about the baseline. Equation (17) gives the quadratic least-squares form for C_Y and C_Z, with θ_e in radians and i ∈ {Y,Z}. Equations (18) and (19) yield R^2 = 0.9966 for C_Y and R^2 = 0.9953 for

C_Z over $-22.5 \leq \theta_e \leq 22.5$ degrees. A piecewise cubic Hermite shape-preserving curve displays the discrete trend from −45 to 45 degrees.

$$C_i(\theta_e) = a_i\theta_e^2 + b_i\theta_e + c_i, \quad i \in \{Y, Z\} \tag{17}$$

$$C_Y = -0.7462\theta_e^2 - 0.4355\theta_e + 1.1299, \quad R^2 = 0.9966 \tag{18}$$

$$C_Z = -0.5011\theta_e^2 + 0.5946\theta_e + 0.4118, \quad R^2 = 0.9953 \tag{19}$$

$$C_{i,\theta}(0) \approx \frac{b^2[C_i(a) - C_i(-a)]}{2a(b^2 - a^2)} - \frac{a^2[C_i(b) - C_i(-b)]}{2b(b^2 - a^2)} \tag{20}$$

The force regressions show that vertical support decreases and lateral loading increases as θ_e moves through the local interval in the positive direction, with appreciable curvature in both responses. A quadratic regression of C_{mx} over the same five points gives $R^2 = 0.7528$ and smooths the local increase at 10 degrees. Accordingly, the pitching moment response is evaluated by central differences at multiple symmetric half-widths, and the shape-preserving curve displays the computed trend. Figure 10 presents the force regressions, discrete pitching moment response, and derivative sensitivity in separate panels.

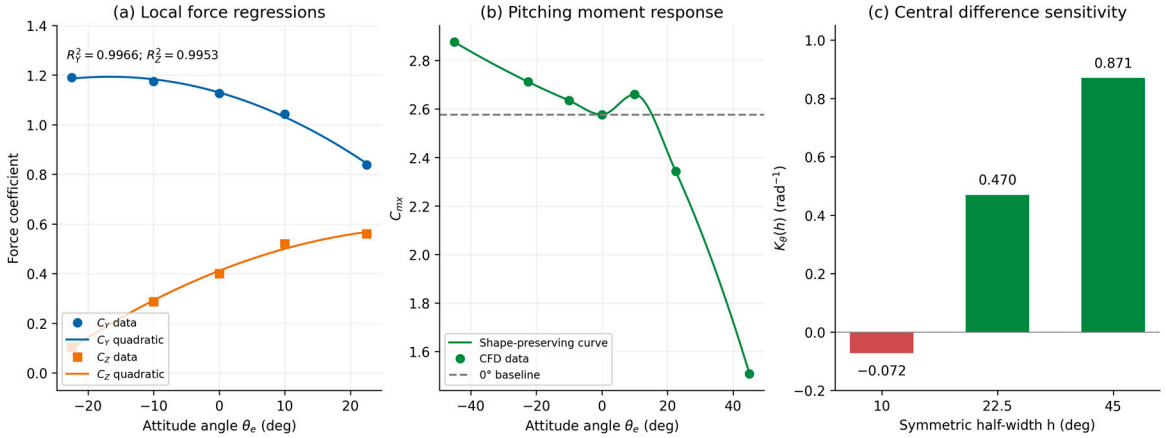

Figure 10. Dimensionless attitude response of the seven rotating cases: (**a**) five-point local quadratic regressions for C_Y and C_Z; (**b**) computed Cmx with a shape-preserving descriptive curve; and (**c**) central difference restoring stiffness sensitivity to the symmetric half-width. In (**a**), blue circles and orange squares denote CY and CZ, and solid curves are their local regressions. In (**b**), green symbols denote computed values, the green curve is shape-preserving, and the dashed line marks the 0-degree baseline. In (**c**), red and green bars denote negative and positive stiffness, respectively.

For the irregularly spaced five-point set at ±10 and ±22.5 degrees, the derivative at 0 degrees is evaluated with the nonuniform central difference expression in Equation (20), where a = 10π/180 rad and b = 22.5π/180 rad. The resulting sensitivities are $C_{Y,\theta} = -0.3578$ rad^{-1}, $C_{Z,\theta} = 0.6918$ rad^{-1}, and $C_{mx,\theta} = 0.2056$ rad^{-1}. The force-derivative signs agree with the local regressions. The positive five-point C_{mx} slope corresponds to $K_\theta < 0$ and characterizes the immediate response as near-neutral to weakly non-restoring.

$$D_i(h) = \frac{C_i(+h) - C_i(-h)}{2h} \tag{21}$$

Equation (21) defines a central difference for each symmetric half-width h and therefore quantifies the effect of disturbance amplitude. The C_{mx} slopes D_{mx}(h) are 0.0722, −0.4699, and −0.8705 rad^{-1} for h = 10, 22.5, and 45 degrees, respectively; the corresponding restoring stiffnesses K_θ(h) are −0.0722, 0.4699, and 0.8705 rad^{-1}. The sign change demonstrates a nonlinear, amplitude-dependent response: the ±10-degree pair is near-neutral to weakly

non-restoring, whereas the ±22.5- and ±45-degree pairs exhibit increasingly strong quasi-steady restoring increments.

$$\Delta C_{mx}(\theta_e) = C_{mx}(\theta_e) - C_{mx}(0) \tag{22}$$

Because $C_{mx}(0)$ is finite, the restoring tendency is evaluated from the moment increment ΔC_{mx} defined by Equation (22). The criterion in Equation (23) is satisfied at −45, −22.5, −10, 22.5, and 45 degrees; the 10-degree increment acts in the disturbance direction. Equation (24) expresses the same bilateral assessment through K_θ(h). The moderate and large disturbance pairs exhibit a quasi-steady static-restoring tendency, while the immediate neighborhood of 0 degrees is near-neutral and contains a shallow local reversal.

$$\theta_e \Delta C_{mx}(\theta_e) < 0 \tag{23}$$

The parameter K_θ is an aerodynamic stiffness derived from prescribed steady loads and characterizes the quasi-steady static-restoring tendency. Dynamic stability additionally depends on mass, moments of inertia, and aerodynamic damping and requires transient or 6DOF calculations together with free-descent experiments.

$$K_\theta(h) = -D_{mx}(h) \tag{24}$$

The resultant force direction is characterized by the lateral offset ratio χ and force angle β in Equations (25) and (26). Across the rotating cases, χ increases from 0.0099 at −45 degrees to 0.6686 at 22.5 degrees and is 0.5452 at 45 degrees; β changes from −0.57 to 33.77 degrees before decreasing to 28.60 degrees as the total load weakens. Thus, the negative-angle cases generally combine stronger vertical support with less lateral offset, whereas positive deflection increases the lateral share of the aerodynamic load.

$$\chi = \frac{|C_Z|}{C_Y} \tag{25}$$

$$\beta = \text{atan2}(C_Z, C_Y) \tag{26}$$

The composite assessment of the seven rotating attitudes uses vertical support, lateral offset, and restoring moment as three indicators. Equation (27) defines the restoring index $R(\theta_e) = -\theta_e \Delta C_{mx}$, whose positive values correspond to moment increments opposing the disturbance. Equation (28) applies min–max normalization to C_Y, χ, and R. The 90-degree case is reported separately as the nonrotating reference.

$$R(\theta_e) = -\theta_e \Delta C_{mx}(\theta_e) \tag{27}$$

$$\hat{x}_j = \frac{x_j - x_{\min}}{x_{\max} - x_{\min}} \tag{28}$$

$$J_j = \frac{1}{3}\left[\hat{C}_{Y,j} + \left(1 - \hat{\chi}_j\right) + \hat{R}_j\right] \tag{29}$$

Equation (29) assigns equal one-third weights to normalized vertical support, the complement of normalized lateral offset, and the normalized restoring index. Table 9 shows that the −45-degree case gives the highest score, J = 0.764, followed by −22.5 degrees. This ranking applies to the seven computed rotating attitudes, the stated normalization range, and the equal-weight setting. Mission-oriented studies may adjust the weights for slow descent, targeted deployment, or disturbance resistance.

Table 9. Equal-weight aerodynamic screening metrics for the seven rotating attitudes.

θ_e	C_Y	χ	R	J	Rank
−45 degrees	1.1884	0.0099	0.2350	0.764	1
−22.5 degrees	1.1901	0.0886	0.0530	0.653	2
−10 degrees	1.1745	0.2440	0.0101	0.552	3
0 degrees	1.1269	0.3554	0.0000	0.475	4
10 degrees	1.0434	0.4987	−0.0145	0.366	6
22.5 degrees	0.8388	0.6686	0.0919	0.248	7
45 degrees	0.2681	0.5452	0.8390	0.396	5

To quantify the load redistribution mechanism using quantities available for every CFD case, the y–z resultant force is written as $F_{yz} = (0, F_y, F_z)$, and an equivalent application point measured from the mass centroid is written as $r_{eq} = (0, \Delta y_{eq}, \Delta z_{eq})$. Infinitely many points on the same force line generate an identical moment. A unique projected representative point is therefore obtained by imposing $r_{eq} \cdot F_{yz} = 0$, which selects the point on the line of action closest to the mass centroid. The x component of $r_{eq} \times F_{yz}$ then gives Equation (30), and Equations (31)–(33) follow:

$$M_x = \Delta y_{\mathrm{eq}} F_z - \Delta z_{\mathrm{eq}} F_y \tag{30}$$

$$\Delta y_{\mathrm{eq}} = \frac{M_x F_z}{F_y^2 + F_z^2} \tag{31}$$

$$\Delta z_{\mathrm{eq}} = -\frac{M_x F_y}{F_y^2 + F_z^2} \tag{32}$$

$$d_\perp = \sqrt{\Delta y_{\mathrm{eq}}^2 + \Delta z_{\mathrm{eq}}^2} = \frac{|M_x|}{\sqrt{F_y^2 + F_z^2}} \tag{33}$$

A positive Δy_{eq} and Δz_{eq} follow the global +y and +z directions, respectively, and $d_\perp$ is the perpendicular distance from the mass centroid to the equivalent y–z plane line of action. The reconstruction uses the total aerodynamic force and moment, including pressure and viscous contributions, and provides an integral measure of the projected load position relative to the centroid. Table 10 lists the values for all eight cases, with 90 degrees reported as the nonrotating broadside reference. Figure 11 shows the corresponding variation with attitude.

Table 10. Equivalent aerodynamic line of action offsets from the mass centroid in the y–z plane.

θ_e (deg)	Condition	$\lvert F_{yz} \rvert$ ($\times 10^{-4}$ N)	Δy_{eq} (mm)	Δz_{eq} (mm)	$d_\perp$ (mm)
−45	Rotating	2.3584	−0.072	−7.260	7.260
−22.5	Rotating	2.3710	0.601	−6.783	6.809
−10	Rotating	2.3992	1.550	−6.352	6.538
0	Rotating	2.3734	2.165	−6.090	6.464
10	Rotating	2.3139	3.054	−6.124	6.844
22.5	Rotating	2.0023	3.872	−5.791	6.966
45	Rotating	0.6061	7.093	−13.011	14.819
90	Nonrotating reference	1.3753	5.633	4.077	6.953

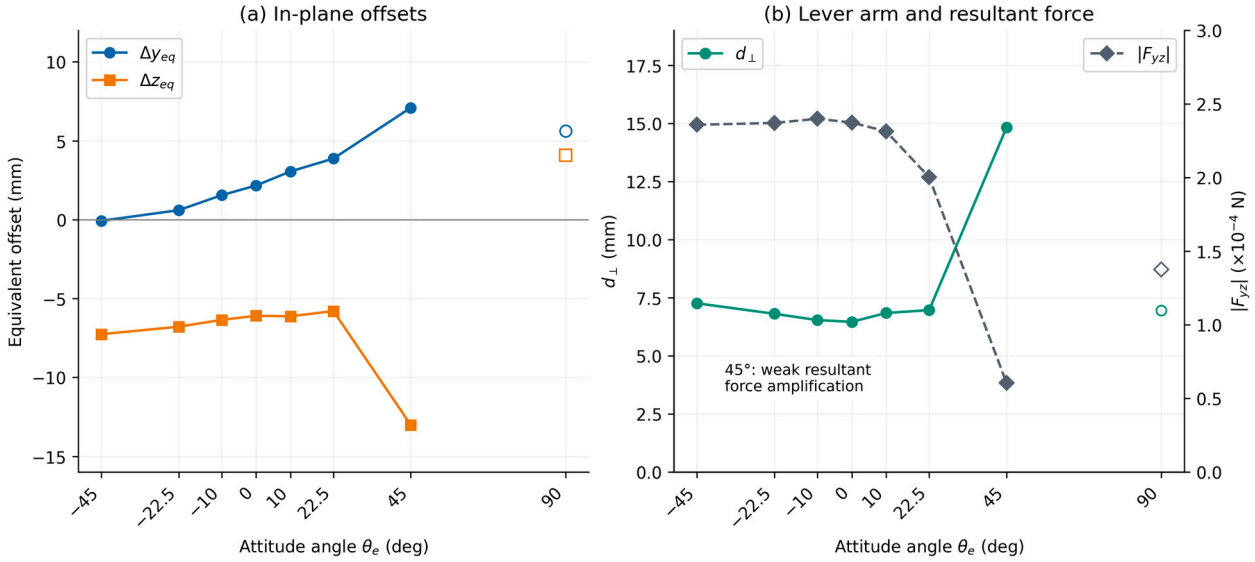

Figure 11. Equivalent aerodynamic line of action reconstruction from the integrated loads: (**a**) in-plane offsets Δy_{eq} and Δz_{eq}; and (**b**) perpendicular distance $d_\perp$ with resultant force magnitude $|F_{yz}|$. Lines connect only the seven rotating CFD cases as visual guides; the 90-degree nonrotating reference is shown by unconnected open markers. Circles and squares in (**a**) distinguish Δyeq and Δzeq; green circles and gray diamonds in (**b**) distinguish d⊥ and |Fyz|.

The equivalent line of action offsets vary with attitude, with line segments connecting the seven rotating CFD results. From −45 to 22.5 degrees, Δy_{eq} increases monotonically from −0.072 to 3.872 mm, while Δz_{eq} remains between −7.260 and −5.791 mm and $d_\perp$ remains within 6.464–7.260 mm. The projected line therefore migrates mainly toward +y while the resultant force direction changes. At 45 degrees, $|F_{yz}|$ decreases to 6.061×10^{-5} N and M_x remains 8.9814×10^{-7} N m, giving $d_\perp$ = 14.819 mm in Equation (33). This value reflects amplification of the equivalent moment arm under weak resultant loading. The nonrotating 90-degree case gives (Δy_{eq}, Δz_{eq}) = (5.633, 4.077) mm and represents broadside loading.

The attitude response is characterized at four complementary levels: local quadratic regressions for C_Y and C_Z over ±22.5 degrees, multi-scale central differences for the pitching moment, shape-preserving curves for the discrete −45-to-45-degree trend, and the equivalent y–z plane line of action describing load migration relative to the mass centroid. Together, these results show a nonlinear, disturbance amplitude-dependent quasi-steady static-restoring tendency and provide the vertical support, lateral offset, and restoring moment inputs used in the equal-weight comparison.

3.4. Surface Pressure Distributions at Different Attitudes

Figure 12 compares surface static pressure distributions at four representative attitudes: the 0-degree rotating baseline, the 45-degree positive bound, the 90-degree nonrotating broadside condition, and the −45-degree negative bound. The intermediate attitudes are characterized by the integrated forces, moments, and equivalent line of action results, while the representative pressure fields clarify the flow mechanisms at the baseline and bounds. High-pressure regions occur mainly on the windward body, near the wing roots, and over portions of the windward wing surfaces; low-pressure regions develop over the leeward surfaces, tips, and root transition zones. Their migration changes F_y, F_z, and M_x simultaneously.

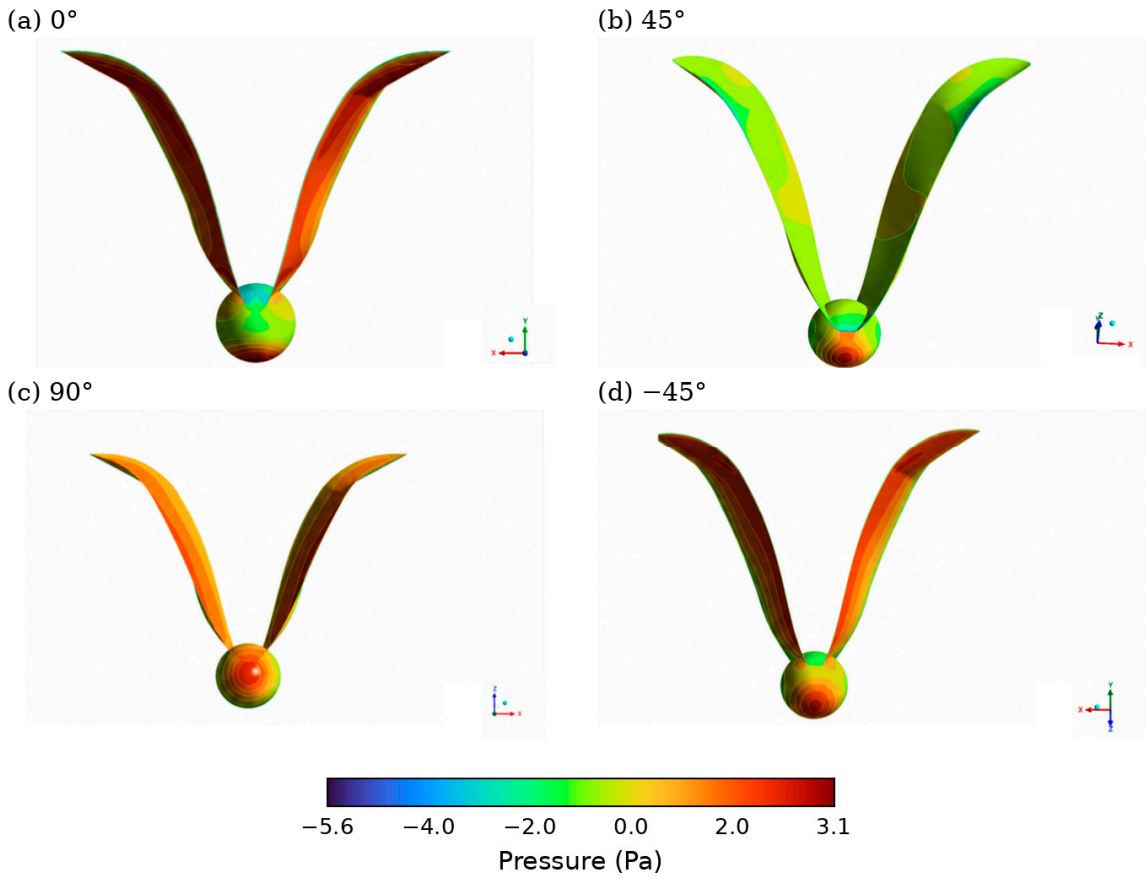

Figure 12. Surface static pressure distributions at four representative attitudes: (**a**) 0 degrees; (**b**) 45 degrees; (**c**) 90 degrees; and (**d**) −45 degrees. All panels use the common pressure scale shown below. Small colored spheres and arrows are coordinate-orientation markers. The views are independently framed; geometric dimensions are given in Table 1.

At −45 degrees, a strong wing surface pressure difference is maintained, and the arrangement of the high- and low-pressure regions produces substantial vertical support with near-cancellation of lateral contributions. At 0 degrees, both wings retain a continuous pressure contrast, while the less balanced left–right distribution produces a finite F_z. At 45 degrees, contraction of the high-pressure region and weakening of the pressure contrast explain the marked loss of vertical support. The projected values follow the same progression: Δy_{eq} changes from −0.072 mm at −45 degrees to 2.165 mm at 0 degrees and 7.093 mm at 45 degrees, and the reduced resultant force at 45 degrees increases $d_\perp$ to 14.819 mm. The 90-degree pressure field is concentrated on the broadside windward region and produces a transverse force whose magnitude exceeds F_y, yielding a lateral transport-dominated load state.

3.5. Streamline Structure and Quasi-Steady Attitude Response

Figure 13 shows colored velocity streamlines at the same four representative attitudes in the following order: 0, 45, 90, and −45 degrees. All panels use a common 0–2.4 m/s scale: red–orange denotes approximately 1.8–2.4 m/s, green–yellow denotes intermediate-speed flow, and blue–cyan denotes low-speed recirculation or vortex core regions. The streamline features are interpreted together with the integrated forces and moments for the eight cases [28,29,32,34].

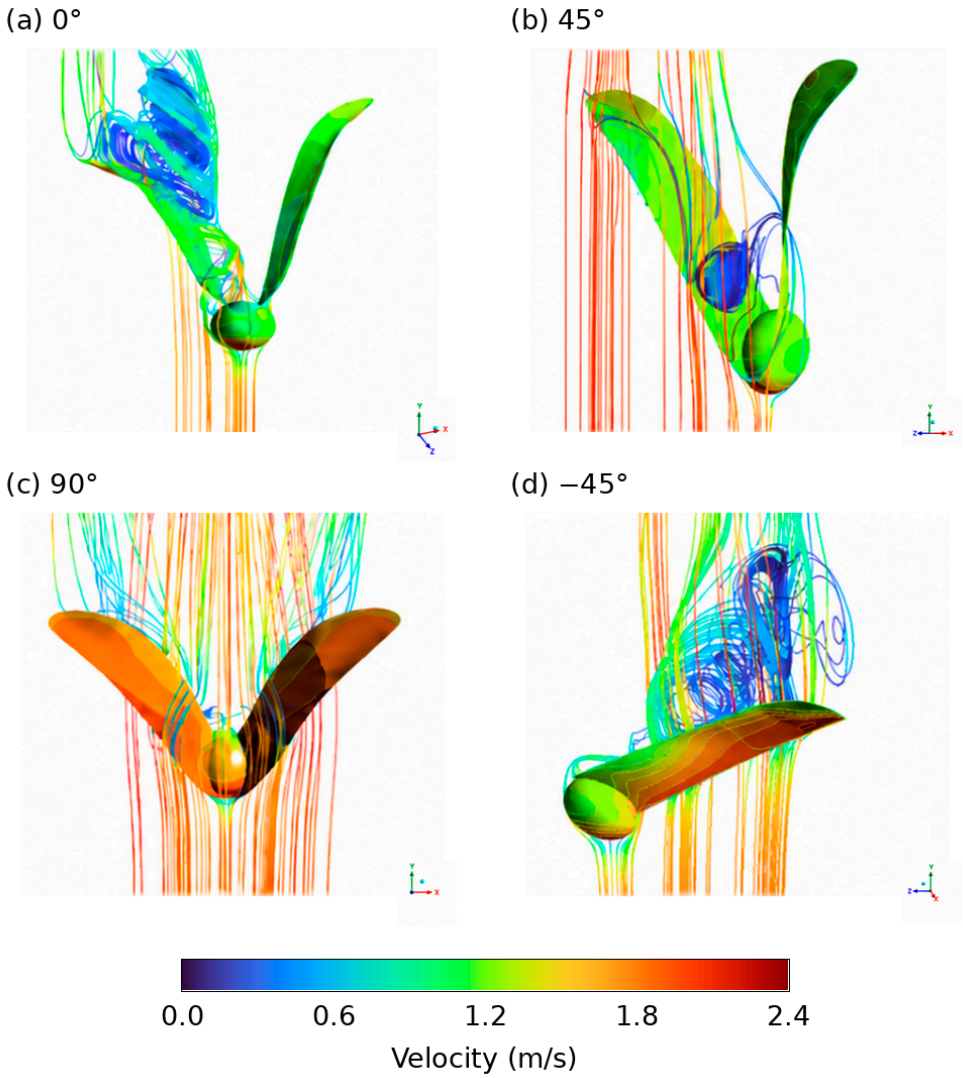

Figure 13. Streamline distributions at four representative attitudes: (**a**) 0 degrees; (**b**) 45 degrees; (**c**) 90 degrees; and (**d**) −45 degrees. Streamline color indicates velocity magnitude on the common scale; the surface colors are retained from the accompanying surface rendering. Coordinate markers are graphical orientation aids.

At 0 degrees, intermediate-to-high-speed flow persists below the body and on the windward side of the wing roots, while a helical low-speed region develops from the root toward the upper wing and near wake. The outer streamlines continue along the wing path, indicating that the separated region preserves effective flow over the paired wings. This organized near-wing flow sustains the substantial aerodynamic load observed at the kinematic baseline.

At 45 degrees, high-speed streamlines pass mainly along the outer wing edge, while a compact low-speed recirculation region concentrates around the opposite wing and body–root junction. The one-sided wake deflection reflects a strongly asymmetric incidence and separation pattern and is consistent with the loss of F_y. Although the 45-degree moment increment has a restoring direction relative to 0 degrees, its reduced vertical support shows why the restoring tendency and overall aerodynamic quality must be evaluated separately.

During nonrotating descent at 90 degrees, most high-speed streamlines pass comparatively directly between the wings and around the body, with only limited low-speed regions near the roots and wake. The large helical recirculation observed in the rotating cases is weakened, and the flow is governed mainly by broadside exposure and local separation.

This case therefore characterizes transverse transport under a different kinematic condition and is excluded from the rotating case restoring assessment.

At −45 degrees, low-speed streamlines form an extensive and coherent helical structure from the wing root region toward the leeward surfaces and near wake, surrounded by intermediate-speed flow. Curled loops near the tips indicate three-dimensional roll-up of the tip shear layers. Relative to the compact one-sided recirculation at 45 degrees, the −45-degree structure remains better organized along the root–wing–wake path. The integrated near-zero F_z indicates that lateral contributions cancel effectively even though the local flow is strongly three-dimensional, while the large F_y confirms that the accelerated flow and low-pressure vortex regions sustain vertical support.

The quasi-steady moment response depends on the joint migration of the equivalent resultant force line and the organized vortex system relative to the mass centroid. The −45- and 45-degree fields show the large deflection asymmetry, and the integrated results at ±10 and ±22.5 degrees characterize the local nonlinearity about 0 degrees. The equivalent offsets quantify the effective moment arm of the integrated loads, the pressure and streamline fields explain the baseline and bounding flow mechanisms, and the multi-scale derivatives describe the pitching response at different disturbance amplitudes.

The combined force, moment, pressure, and streamline results give the highest equal-weight composite score to −45 degrees among the seven rotating attitudes. The 0-degree case is the kinematic baseline; 10 degrees exhibits a near-baseline non-restoring moment increment; and 22.5 and 45 degrees exhibit restoring increments accompanied by progressively weaker vertical support. The nonrotating 90-degree case represents broadside descent, and its large transverse force promotes lateral transport.

4. Conclusions

A three-dimensional model of an *H. hainanensis*-inspired double-winged samara was established, and steady MRF simulations compared quasi-steady aerodynamic forces, moments, surface pressure distributions, and streamline structures at seven prescribed rotating attitudes (−45, −22.5, −10, 0, 10, 22.5, and 45 degrees) and a nonrotating 90-degree reference. The loads were sensitive to attitude; vertical support, lateral force, moment about the x axis, and near-wing flow organization all varied with orientation.

Among the seven rotating cases, the −45-degree case combines $F_y = 2.3583 \times 10^{-4}$ N with $F_z = -2.3398 \times 10^{-6}$ N and attains the highest equal-weight composite score, $J = 0.764$. The −22.5-degree case gives the maximum rotating case vertical force, $F_y = 2.3617 \times 10^{-4}$ N. The 0-degree case provides the kinematic baseline with $F_y = 2.2363 \times 10^{-4}$ N, while vertical support decreases markedly at 45 degrees. In the nonrotating 90-degree case, $F_z = -1.1141 \times 10^{-4}$ N promotes transverse transport and may increase seed dispersal.

The dominant moment component is M_x about the x axis. Five-point force regressions over ±22.5 degrees give R^2 values of 0.9966 and 0.9953 for C_Y and C_Z, respectively, while the pitching moment response is distinctly nonlinear. Central differences using ±10-, ±22.5-, and ±45-degree pairs give restoring stiffnesses of −0.072, 0.470, and 0.871 rad^{-1}. The small disturbance pair is near-neutral to weakly non-restoring, whereas the moderate and large disturbance pairs exhibit quasi-steady restoring increments.

The pressure and streamline fields show that attitude-dependent migration of high- and low-pressure regions and root–wing–wake vortical structures changes the direction and effective moment arm of the resultant load. The equivalent y–z plane line of action moves from $(\Delta y_{eq}, \Delta z_{eq}) = (-0.072, -7.260)$ mm at −45 degrees to (3.872, −5.791) mm at 22.5 degrees, while $d_\perp$ remains within 6.464–7.260 mm. At 45 degrees, the reduced resultant

load increases $d_{\perp}$ to 14.819 mm, reflecting effective moment arm amplification under weak loading. The 90-degree case represents a lateral load-dominated broadside flow state.

The bio-inspired value of the double-winged samara arises from aerodynamic–moment coupling among wing deployment, tip bending and twist, root mounting, migration of the equivalent resultant force line, and concentration of mass in the seed body. Practical configurations should coordinate wing shape, root attachment, and mass distribution so that the resultant aerodynamic force acts through a favorable lever arm relative to the center of gravity. Root stiffness and wingtip bending or twist can also be selected to maintain effective near-wing pressure distributions under attitude disturbances. For low-Reynolds-number micro aerial vehicles, unpowered deployment nodes, and lightweight environmental sensors, the normalized vertical force coefficient, lateral offset ratio, and local static-restoring stiffness can be combined with task-specific weights. Wingtip bending and twist, wing-fold angle, root mounting angle and stiffness, wing thickness, and equivalent seed body mass distribution provide the principal variables for configurations that balance slow descent, disturbance resistance, and structural simplicity.

Future work should first refine the attitude sampling near 0 degrees and over the negative angle range, extend the rotational speed assessment to additional attitudes, and quantify uncertainty in the moment derivatives. Transient sliding-mesh simulations, 6DOF free-descent calculations, and experiments can then resolve attitude recovery, rotational speed development, and unsteady vortex dynamics. Response surfaces, surrogate models, or intelligent optimization algorithms may be used to identify improved attitude and geometric combinations. The resulting aerodynamic–moment coupling can support manufacturable bio-inspired wings and passive stabilization structures for emergency descent or unpowered recovery of micro aerial vehicles, deployment of environmental monitoring and precision agriculture sensor nodes, dispersal of lightweight aerial nodes in disaster areas, and low-cost distributed monitoring systems [9,22–24,27].

Author Contributions: Conceptualization, W.W.; methodology, X.L.; software, X.L.; validation, X.L.; formal analysis, X.L.; investigation, X.L.; resources, X.L.; data curation, X.L.; writing—original draft preparation, X.L.; writing—review and editing, X.L.; visualization, X.L.; project administration, X.L.; supervision, W.W. All authors have read and agreed to the published version of the manuscript.

Funding: This research received no external funding.

Data Availability Statement: The data presented in this study are available in the tables and figures of this article.

Acknowledgments: The authors used ChatGPT-5.5 (OpenAI) for translation and language editing. The authors reviewed and edited the output and take full responsibility for the content of this publication.

Conflicts of Interest: The authors declare no conflict of interest.

Abbreviations

The following abbreviations are used in this manuscript:

Abbreviation	Definition
6DOF	Six degrees of freedom
CFD	Computational fluid dynamics
MAV	Micro aerial vehicle
MRF	Multiple-reference-frame
RANS	Reynolds-averaged Navier–Stokes
SST	Shear stress transport

References

1. Di Luca, M.; Mintchev, S.; Su, Y.; Shaw, E.; Breuer, K. A bioinspired separated-flow wing provides turbulence resilience and aerodynamic efficiency for miniature drones. *Sci. Robot.* **2020**, *5*, eaay8533. [CrossRef] [PubMed]
2. Yao, Y.; Ma, D.; Zhang, L.; Yang, X.; Yu, Y. Aerodynamic optimization and analysis of a low-Reynolds-number propeller with a Gurney flap for an ultra-high-altitude unmanned aerial vehicle. *Appl. Sci.* **2022**, *12*, 3195. [CrossRef]
3. Traub, L.W.; Coffman, C. Efficient low-Reynolds-number airfoils. *J. Aircr.* **2019**, *56*, 1987–2003. [CrossRef]
4. Lurans, E.; Alhinai, A.; Viswanathan, H. Aerodynamics of corrugated wings: Past, present, and future. *Aerospace* **2025**, *12*, 262. [CrossRef]
5. Wang, Z.; Kan, Z.; Li, H.; Li, D.; Zhao, S.; Tu, Z. Parametric study on aerodynamic performance of a flapping wing rotor MAV capable of sustained flight. *Aerospace* **2022**, *9*, 551. [CrossRef]
6. Barroso Barderas, E.; Bardera Mora, R.; Rodriguez-Sevillano, Á.A.; Matías García, J.C. Numerical analysis of bioinspired tails in a fixed-wing micro air vehicle. *Aerospace* **2023**, *10*, 793. [CrossRef]
7. Bai, S.; He, Q.; Chirarattananon, P. A bioinspired revolving-wing drone with passive attitude stability and efficient hovering flight. *Sci. Robot.* **2022**, *7*, eabg5913. [CrossRef] [PubMed]
8. Johnson, K.; Arroyos, V.; Ferran, A.; Villanueva, R.; Yin, D.; Elberier, T.; Aliseda, A.; Fuller, S.; Iyer, V.; Gollakota, S. Solar-powered shape-changing origami microfliers. *Sci. Robot.* **2023**, *8*, eadg4276. [CrossRef] [PubMed]
9. Kim, B.H.; Li, L.; Kim, J.-T.; Park, Y.; Jang, H.; Wang, X.; Xie, Z.; Won, S.M.; Yoon, H.-J.; Lee, G.; et al. Three-dimensional electronic microfliers inspired by wind-dispersed seeds. *Nature* **2021**, *597*, 503–510. [CrossRef] [PubMed]
10. Sunada, S.; Ide, A.; Hoshino, Y.; Okamoto, M. A study of autorotating plant seeds. *J. Theor. Biol.* **2015**, *386*, 55–61. [CrossRef] [PubMed]
11. Jung, B.K.; Rezgui, D. Sectional leading-edge-vortex lift and drag coefficients of autorotating samaras. *Aerospace* **2023**, *10*, 414. [CrossRef]
12. Nave, G.K., Jr.; Hall, N.; Somers, K.; Davis, B.; Gruszewski, H.; Powers, C.; Collver, M.; Schmale, D.G., III; Ross, S.D. Wind dispersal of natural and biomimetic maple samaras. *Biomimetics* **2021**, *6*, 23. [CrossRef] [PubMed]
13. Lee, E.-J.; Lee, S.-J. Effect of initial attitude on autorotation flight of maple samaras (*Acer palmatum*). *J. Mech. Sci. Technol.* **2016**, *30*, 741–747. [CrossRef]
14. Ortega-Jimenez, V.M.; Kim, N.S.-W.; Dudley, R. Superb autorotator: Rapid decelerations in impulsively launched samaras. *J. R. Soc. Interface* **2019**, *16*, 20180456. [CrossRef] [PubMed]
15. Chen, T.; Lan, S. Numerical analysis of dynamic stability of falling maple samaras. *Acta Mech. Sin.* **2022**, *38*, 322111. [CrossRef]
16. McConnell, J.; Das, T. Reduced-order modeling of an autorotating samara for steady-state and dynamic analysis. *IFAC-PapersOnLine* **2022**, *55*, 68–73. [CrossRef]
17. Schaeffer, B.M.; Truscott, T.T.; Dickerson, A.K. Maple samaras recover autorotation following raindrop collisions. *Proc. Natl. Acad. Sci. USA* **2025**, *122*, e2422641122. [CrossRef] [PubMed]
18. Jung, B.K.; Rezgui, D. Experimental study into the effects of pitch and coning angles on the flight performance of the natural samara. *R. Soc. Open Sci.* **2024**, *11*, 240758. [CrossRef] [PubMed]
19. Schaeffer, B.M.; Truman, S.S.; Truscott, T.T.; Dickerson, A.K. Maple samara flight is robust to morphological perturbation and united by a classic drag model. *Commun. Biol.* **2024**, *7*, 248. [CrossRef] [PubMed]
20. Hou, Z.-B.; Zhang, J.-D.; Li, Y.-D.; Jia, Y.-X.; Huang, W.-X. Aerodynamic significance of mass distribution on diverse samara descent behaviors. *Commun. Eng.* **2025**, *4*, 129. [CrossRef] [PubMed]
21. Liu, C.; Feng, C.; Liu, L.; Wang, T.; Zeng, L.; Li, J. Aerodynamic shape optimization of a *Pterocarya stenoptera* seed-based biomimetic aircraft using a neural network. *Aerosp. Sci. Technol.* **2024**, *155*, 109737. [CrossRef]
22. Arya, S.; Spíchal, L.; Zbořil, R. Flying seed-inspired sensors for remote environmental monitoring on Earth and beyond. *Trends Biotechnol.* **2026**, *44*, 1214–1229. [CrossRef] [PubMed]
23. Iyer, V.; Gaensbauer, H.; Daniel, T.L.; Gollakota, S. Wind dispersal of battery-free wireless devices. *Nature* **2022**, *603*, 427–433. [CrossRef] [PubMed]
24. Cikalleshi, K.; Nexha, A.; Kister, T.; Ronzan, M.; Mondini, A.; Mariani, S.; Kraus, T.; Mazzolai, B. A printed luminescent flier inspired by plant seeds for eco-friendly physical sensing. *Sci. Adv.* **2023**, *9*, eadi8492. [CrossRef] [PubMed]
25. Polonelli, T.; Muller, H.; Kong, W.; Fischer, R.; Benini, L.; Magno, M. Aerosense: A self-sustainable and long-range Bluetooth wireless sensor node for aerodynamic and aeroacoustic monitoring on wind turbines. *IEEE Sens. J.* **2023**, *23*, 715–723. [CrossRef]
26. Chilson, P.B.; Bell, T.M.; Brewster, K.A.; Britto Hupsel de Azevedo, G.; Carr, F.H.; Carson, K.; Doyle, W.; Fiebrich, C.A.; Greene, B.R.; Grimsley, J.L.; et al. Moving towards a network of autonomous UAS atmospheric profiling stations for observations in the Earth's lower atmosphere: The 3D Mesonet concept. *Sensors* **2019**, *19*, 2720. [CrossRef] [PubMed]
27. Bell, T.M.; Greene, B.R.; Klein, P.M.; Carney, M.; Chilson, P.B. Confronting the boundary-layer data gap: Evaluating new and existing methodologies of probing the lower atmosphere. *Atmos. Meas. Tech.* **2020**, *13*, 3855–3872. [CrossRef]

28. Arranz, G.; Gonzalo, A.; Uhlmann, M.; Flores, O.; Garcia-Villalba, M. A numerical study of the flow around a model winged seed in autorotation. *Flow Turbul. Combust.* **2018**, *101*, 477–497. [CrossRef]
29. Arranz, G.; Moriche, M.; Uhlmann, M.; Flores, O.; Garcia-Villalba, M. Kinematics and dynamics of the autorotation of a model winged seed. *Bioinspir. Biomim.* **2018**, *13*, 036011. [CrossRef] [PubMed]
30. Fauli, R.A.; Rabault, J.; Carlson, A. Effect of wing-fold angles on the terminal descent velocity of double-winged autorotating seeds, fruits, and other diaspores. *Phys. Rev. E* **2019**, *100*, 013108. [CrossRef] [PubMed]
31. Rabault, J.; Fauli, R.A.; Carlson, A. Curving to fly: Synthetic adaptation unveils optimal flight performance of whirling fruits. *Phys. Rev. Lett.* **2019**, *122*, 024501. [CrossRef] [PubMed]
32. Liu, C.; Wang, T.; Zeng, L.; Li, J.; Shao, X. Effects of wing loading on the aerodynamic characteristics of autorotating maple seeds. *Phys. Fluids* **2024**, *36*, 031908. [CrossRef]
33. Song, Y.-B.; Shen-Tu, X.-L.; Dong, M. Intraspecific variation of samara dispersal traits in the endangered tropical tree *Hopea hainanensis* (Dipterocarpaceae). *Front. Plant Sci.* **2020**, *11*, 599764. [CrossRef] [PubMed]
34. Liu, C.; Zeng, L.; Li, J.; Shao, X. Effects of wings number on the flight performance of autorotating seeds. *Phys. Fluids* **2025**, *37*, 011902. [CrossRef]
35. ANSYS, Inc. *Ansys Fluent Theory Guide: Modeling Flows Using Multiple Reference Frames and Sliding Meshes*; ANSYS, Inc.: Canonsburg, PA, USA, 2024.
36. Kutty, H.A.; Rajendran, P. 3D CFD simulation and experimental validation of small APC slow flyer propeller blade. *Aerospace* **2017**, *4*, 10. [CrossRef]
37. Menter, F.R. Two-equation eddy-viscosity turbulence models for engineering applications. *AIAA J.* **1994**, *32*, 1598–1605. [CrossRef] [PubMed]
38. Çalışkan, M.E.; Kaya, F.; Sabırlı, M.U.; Karagoz, I. Design of a biomimetic wing from maple samara and investigation of the aerodynamic performance. *Phys. Fluids* **2023**, *35*, 095104. [CrossRef]

Disclaimer/Publisher's Note: The statements, opinions and data contained in all publications are solely those of the individual author(s) and contributor(s) and not of MDPI and/or the editor(s). MDPI and/or the editor(s) disclaim responsibility for any injury to people or property resulting from any ideas, methods, instructions or products referred to in the content.